SYNTHESIS AND CHARACTERIZATION OF BULK SINGLE CRYSTAL HEXAGONAL BORON NITRIDE FROM METAL SOLVENTS

by

BENJAMIN CLUBINE

B.S., Kansas State University, 2010

A THESIS

submitted in partial fulfillment of the requirements for the degree

MASTER OF SCIENCE

Department of Chemical Engineering
College of Engineering

KANSAS STATE UNIVERSITY
Manhattan, Kansas

2012

Approved by:

Major Professor
Dr. James H. Edgar

Copyright

Abstract

Boron nitride is a purely synthetic material that has been known for over 150 years but only recently has sparked interest as a semiconductor material due to its potential in ultraviolet lasing and neutron detection. Thin-layer hexagonal boron nitride (hBN) is probably most attractive as a complementary material to graphene during its intense research endeavors. But for hBN to be successful in the realm of semiconductor technology, methods for growing large single crystals are critical, and its properties need to be accurately determined.

In this study, hBN crystals were grown from metal solvents. The effects of soak temperature, soak time, source materials and their proportions on hBN crystal size and properties were investigated. The largest crystals of hBN measured five millimeters across and about 30 micrometers thick by precipitation from BN powder dissolved in a nickel-chromium solvent at 1700°C. High temperatures promoted outward growth of the crystal along the a-axis, whereas low temperatures promoted growth along the c-axis. Crystal growth at high temperatures also caused bulk hBN to adopt a triangular habit rather than a hexagonal one. A previously unreported method of synthesizing hBN was proven successful by substituting BN powder with elemental boron and a nitrogen ambient.

XRD and Raman spectroscopy confirmed hBN from solution growth to be highly crystalline, with an 8.0 cm^{-1} FWHM of the Raman peak being the narrowest reported. Photoluminescence spectra exhibited peaks mid-gap and near the band edge, suggesting impurities and defects in the hBN samples. However, high-purity reactants and post-growth annealing showed promise for synthesizing semiconductor-grade hBN.

Several etchants were explored for defect-selective etching of hBN. A molten eutectic mixture of KOH/NaOH was the most effective defect-selective etchant of hBN at temperatures of 430-450°C for about one minute. The two prevalent hexagonal etch pit morphologies observed were deep, pointed-bottom pits and shallow, flat-bottom pits. TEM and SAED confirmed basal plane twists and dislocations in hBN crystals, but due to the highly anisotropic nature of hBN, their existence may be inevitable no matter the growth technique.

Table of Contents

List of Figures

List of Tables

Acknowledgements

I would like to first thank my advisor, Dr. James Edgar, for all of his support and insight during this project. My committee members, Dr. Larry Glasgow, Dr. Vikas Berry, and Dr. Andrew Rys were also instrumental in my success both in the laboratory and in the classroom. I had the pleasure of working with and getting to know several students in my research group including Clinton Whiteley, Yi Zhang, Ugo Nwagwu, Tashfin Hossain, Daming Wei, and Clint Frye. Their assistance inside the lab and camaraderie outside of the lab mean the world to me. I would also like to thank Ashley Mayo, Chris Mehrer and Kevin Cooper for their help with experiments and analyses. Too numerous to name here are the faculty and staff of the Department of Chemical Engineering who were a pleasure to work with for the six years I spent at K-State as both an undergraduate and graduate student.

Much of this work would not have been possible without the kind support and generosity of many people. Our collaborators, Dr. Hongxing Jiang and Jingyu Lin, provided invaluable photoluminescence data. Qiang "Charles" Ye of the Department of Bioengineering at the University of Kansas was kind enough to allow me access to their Raman microscope; many thanks to Kabeer Jasuja for his help collecting the Raman data. The differential-scanning calorimetry data was generously provided by the Ames Laboratory at Iowa State University. I am thankful for the advice and training that Dr. Dan Boyle provided me with the scanning electron microscope system. The transmission electron microscope images would not have been possible without the very generous support of Karthik Chinnathambi at Boise State University; his thoughts and explanations are also greatly appreciated. A heart-felt thanks goes to Ben Montag and the S.M.A.R.T. lab at K-State for their kind help and support.

Last, but certainly not least, I would like to thank my family for their love and moral support: my parents, Harry and Kathy; my brother Tyler; and my wife Kari, who has been incredibly patient and understanding during my academic studies.

Dedication

To my wife and family.

Chapter 1 - Introduction

Boron nitride (BN) is a synthetic compound discovered by Balmain(*1*) in 1842 when he reacted boric oxide with potassium cyanide. However, industrial uses for BN were not realized for another 100 years.(*2*) The microcrystalline powder form of BN has many uses as a lubricant or coating when chemical inertness at high temperatures is required. BN powder is also used extensively as a filler material and a precursor for other boron compounds. The hot-pressed form of boron nitride (HPBN) is especially useful as a refractory material. Properties like its high thermal conductivity, high thermal shock resistance, and machining ease make HPBN invaluable in furnaces, reactors, and other high-temperature applications.(*3*)

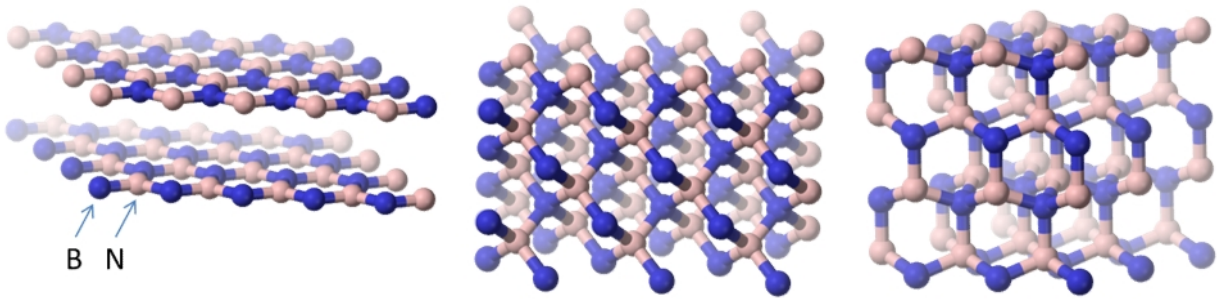

Figure 1-1 Three main crystal structure modifications of boron nitride: hBN (left), cBN (middle), and wBN (right).

Crystalline boron nitride can assume many forms, and to be clear, these forms are labeled with an appropriate prefix. Figure 1-1 illustrates the common structures of crystalline boron nitride that exhibit long-range order: hexagonal (hBN), cubic (cBN), and wurtzitic (wBN). (From this point forward, BN as written will refer to all boron nitride phases in general.) hBN is a soft, low density modification of BN and is composed of layers of flat six-atom sp^2-hybridized hexagonal rings (three atoms boron and three atoms nitrogen alternating) with the rings stacked perfectly atop each other in alternating fashion AA'AA' (boron atop nitrogen atop boron…). cBN is one of the hard, high density modifications of BN and adopts the zinc blende structure with stacking sequence ABCABC. Every atom is bonded to four others of the opposite element (boron to four nitrogens and nitrogen to four borons), giving an sp^3 hybridization structure. wBN is the other hard, high density BN modification in which the unit cell is hexagonal but possesses sp^3 hybridization bonding among the constituent atoms. Although the wurtzite

structure is common among other group III-nitride compounds, wBN is a rare and metastable structure for boron nitride. The BN phase diagram from Bundy and Wentorf(*4*), subsequently revised by Corrigan and Bundy(*5*), shows cBN to be the thermodynamically stable phase up to about 1500°C.

The layered structure of hBN makes it prone to alternate stacking arrangements. Figure 1-2 depicts a few such modifications. Rhombohedral BN (rBN) is similar to hBN and can have equally long-range order, but the layered planes of hBN are translated parallel to each other while maintaining boron-nitrogen-boron… stacking sequence among layers (ABCABC). The meaning of long-range order in hBN and rBN is that all layers are parallel and appropriately oriented with respect to the c-axis. In contrast, turbostratic BN (tBN) has short-range order where many layers are tilted, rotated and translated with respect to each other and borders on polycrystallinity. A commonly encountered form of hBN is pyrolytic BN (pBN) typically prepared by chemical vapor deposition; it adopts the layered hBN structure but is by no means single crystal since it has many grains and reduced long-range order.

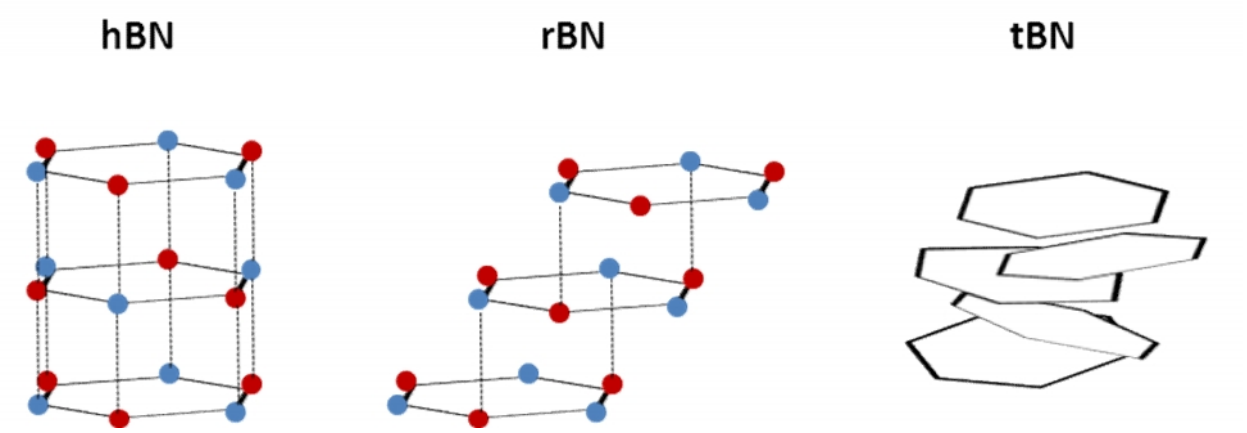

Figure 1-2 Crystal structures of hBN, rBN and tBN.

BN shares many structural similarities with those of carbon allotropes— hBN to graphite, cBN to diamond, BN nanotubes to carbon nanotubes, monolayer hBN to graphene, etc. Table 1-1 lists some selected properties of hBN, cBN, graphite and diamond. The BN phases are also isoelectronic with their carbon phase counterparts. However, some properties (such as the electrical properties of hBN and graphite/graphene) are drastically different. Because of their many similarities and yet stark differences, hBN and graphite/graphene are said to be complementary. For instance, whereas graphene is an excellent electrical conductor with a zero band gap, hBN is quite insulating with a band gap close to 6 eV.(*6*, *7*) In fact to date, the highest

reported electron mobility in graphene when supported on a substrate was with monolayer hBN.(*8*) The structures of graphene and hBN match so well that little distortion of the graphene sheet occurs, and the large band gap of hBN decreases the interaction of electrons with the substrate, resulting in a reduction of electron scattering within the graphene layer and, hence, increased electron mobility.

Table 1-1 Selected properties of boron nitride and carbon analogs.(*2, 6, 9–12*)

Property	hBN	graphite	cBN	diamond
Crystal structure	Hexagonal	Hexagonal	Cubic	Cubic
Lattice constant (Å)	a = 2.504 c = 6.661	a = 2.461 c = 6.708	3.615	3.567
Density (g/cm^3)	2.34	2.2	3.45	3.515
Mohs hardness	1.5	1-2	9.5	10
Band gap (eV)	5.971 (direct)	0 (semimetal)	6.4 (indirect)	5.4 (indirect)
Electrical conductivity $[(\Omega cm)^{-1}]$	a: $< 10^{-15}$ c: $< 10^{-16}$	a: 9.8×10^{-4} c: 4.1×10^{-3}	$\sim 10^{-13}$	$\sim 10^{-18}$
Thermal conductivity (W/m/K)	a: 63 c: 1.5	a: 250 c: 80	~400-700	~2000
Linear thermal expansion (K^{-1})	a: -2.9×10^{-6} c: 40.5×10^{-6}	a: -1.2×10^{-6} c: 25.9×10^{-6}	$1.2\text{-}1.9 \times 10^{-6}$	0.8×10^{-6}

Since its constituent atoms reside in Groups III and V of the periodic table, crystalline boron nitride is appropriately called a III-V compound semiconductor and hence related to other III-V compounds such as AlN and GaAs. III-V compounds in general have garnered much interest in the semiconductor and material science fields for their often superior electrical, thermal and structural properties compared to the ubiquitous silicon semiconductor. For instance, while silicon has an indirect band gap, many of the III-V compounds have direct band gaps that make optical applications like light-emitting diodes (LEDs) and lasers much more

energy efficient. Some III-V compounds like AlN and cBN have much higher thermal conductivities than silicon which reduces constraints like overheating and the need for complex cooling systems in high-power devices.

Hexagonal boron nitride has thus far been a poor material for electronic devices mainly because of difficulty in obtaining high-quality crystalline samples. The most prevalent (poly)crystalline form of boron nitride is pBN primarily synthesized by chemical vapor deposition. Several important properties of hBN listed in Table 1-1 were collected from pBN, but important electrical properties like charge carrier mobility and electrical conductivity are significantly dependent on crystal quality. Thus, their ultimate values remain unknown. Therefore, to address the need for quality specimens necessary for electrical device fabrication, this work focuses on the synthesis of bulk, single crystal hBN.

Potential Applications for hBN

hBN holds promise in many areas of electronics as described by Yamaguchi(*13*). It can be a protective coating to prevent chemical attack by other materials; a boron diffusion source for silicon; or a gate insulator for field-effect transistors. With the advent of graphene field-effect transistors, hBN has shown to be an excellent gate dielectric and substrate that provides a smooth and flat surface necessary for maximum carrier mobility in graphene sheets.(*8*, *14*)

While visible light-emitting diodes (LEDs) and laser diodes are well-established, materials for ultraviolet (UV) emission have only recently come of age. The III-V compound gallium nitride (GaN) is a prominent material in violet laser diodes, and their most widespread use is to read discs in Blu-ray players. But many UV applications exist in medicine, security/counterfeiting, and antimicrobial/sterilization methods all of which could benefit from UV LEDs.(*15*) UV emission from hBN has been reported(*6*, *16*) with wavelengths between 215 nm and 227 nm depending on crystal quality. Since most UV devices still rely on conventional UV lamps, hBN has potential to become a dominant, low power solid-state UV emitter.(*17*)

Another potential application of boron nitride is in neutron detection. As imported goods cross the border into the U.S., many are inspected for radioactive materials to prevent domestic attacks with smuggled nuclear material. Gas-filled neutron detectors are the most prevalent systems today. The medium most often used in gas-filled detectors is ^{3}He, a rare isotope of helium (~0.0001% on earth) that strongly interacts with thermal neutrons because of its large

neutron capture cross-section of about 5330 barns.(*18*) However, ^{3}He detectors are declining in popularity because of increasing prices. In the past, ^{3}He was relatively cheap owing to its formation from decaying tritium in nuclear weapon stockpiles. As these stockpiles decrease due to nuclear disarmament agreements, the supply of ^{3}He has dwindled and only covered about a third of demand in 2009.(*19*) An inherent disadvantage of gas-filled neutron detectors in general is their low efficiency.(*20*) Bulky, pressurized tubes are necessary to generate detectable electrical signals when a neutron interaction occurs, making the device delicate and expensive. Therefore, new approaches to neutron detection are currently active areas of research.

Solid-state neutron detectors offer higher efficiencies with a more sturdy and compact design, provided an appropriate material for neutron detection is incorporated into the device.(*20*) Boron nitride is such a material because the ^{10}B isotope has a neutron capture cross section of about 3840 barns.(*18*) A neutron interacts with ^{10}B by the reaction in Equation 1-1

$$^{10}B + {}^{1}n \longrightarrow {}^{7}Li + {}^{4}\alpha + E \qquad (1\text{-}1)$$

where 94% of the time the ^{7}Li particle is in an excited state and E = 2310 keV, whereas 6% of the time the ^{7}Li particle is formed in its ground state and E = 2790 keV.(*18*) Since boron in its natural abundance is about 20% ^{10}B and 80% ^{11}B, neutron detection is possible without further isotopic enrichment. However, ^{10}B-enriched BN would reduce the material thickness required for completely capturing neutrons, making charge collection (and, hence, signal detection) in a material with low carrier mobilities easier.(*20*) Some other properties of boron nitride that are intriguing for neutron detection are its low effective atomic number (10.8 and 14 for natural boron and nitrogen, respectively) and high dielectric strength (>140 eV/nm).(*20*) The former property is useful for discriminating neutron emission from gamma radiation since low-Z nuclei are more transparent to gamma rays than heavier nuclei.(*20*) The latter property is important since high applied voltages are typically necessary to operate the device with maximum charge-collection capability.

While conventional solid-state neutron detectors made of silicon and a neutron-capturing material have been around for decades(*21*), they are plagued by low efficiencies. The first were layered structures as in Figure 1-3a. An incident neutron entering the neutron-capturing layer (e.g. boron or boron compound) strikes a ^{10}B atom and ejects ^{7}Li and an alpha particle. The alpha particle must then traverse to the semiconductor layer (e.g. silicon) where it interacts with the silicon atoms to produce electron-hole pairs and, thus, a detectable electrical signal. The

separated neutron-capture and charge-collection layers are responsible for the device's poor efficiency, and their thicknesses are critical; the boron layer must be thick enough to provide enough ^{10}B centers for neutron capture, but thin enough to allow the generated alpha particles to escape the boron layer into the silicon layer where an electrical signal can be detected. Efforts to overcome inefficiency of the layered devices have led to pillared devices as in Figure 1-3b where thin alternating layers of boron and silicon are stacked side-by-side to increase the likelihood of neutron capture and alpha particle-spawned electrical signals.(*22*) The efficiency of these devices is still below 10%.(*22*)

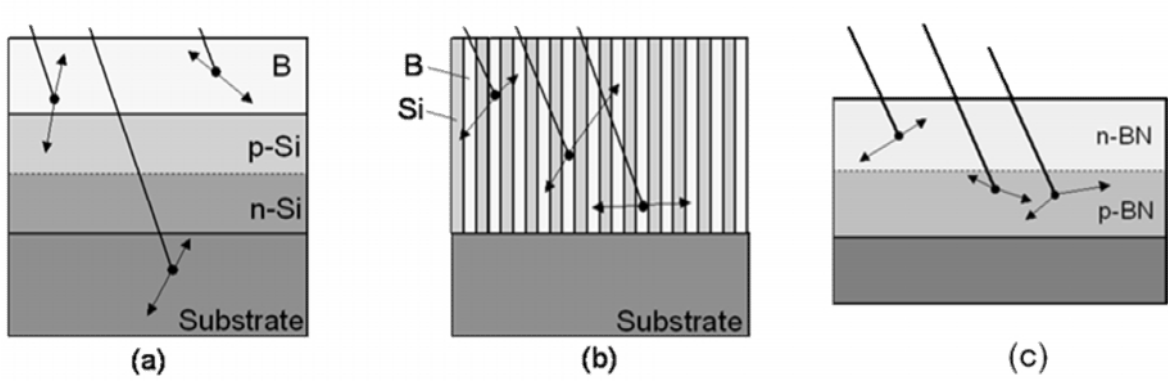

Figure 1-3 Schematics of neutron detector devices employing (a) a boron conversion layer atop a silicon pn junction diode; (b) alternating narrow pillars of boron and silicon layers; (c) single crystal hBN as both the neutron-capturing and semiconductor layer. The dots represent ^{10}B-neutron reaction sites, and the arrows represent dispersion of the daughter products postreaction, i.e. ^{7}Li and $^{4}\alpha$.

The maximum theoretical efficiency is achieved if the neutron-capturing and charge-collection layers are integrated into a single layer (Figure 1-3c). This implies the need for a material that is a boron-containing semiconductor, and many such materials have been tested including boron carbide(*23*), boron phosphide(*24*) and pBN(*20, 25*). While the efficiencies of the pBN devices tested by both Doty(*20*) and McGregor et al.(*25*) were quite low, this is most likely attributable to the polycrystalline nature of pBN. Bulk, single-crystal hBN should exhibit improved charge transport properties versus pBN and is thus the focus of this study. Growing suitable hBN crystals is discussed next.

Crystal Growth Methods

By far, chemical vapor deposition (CVD) has been the most common method to synthesize hBN over the decades. In this process, chemical precursors containing boron and nitrogen flow through a reaction chamber where they are heated and deposited via chemical reaction onto a substrate. Some common precursors are trifluoroborane(*26*), trichloroborane(*27*) and diborane(*28*) with ammonia. The quality of hBN films made by CVD is dependent on temperature, pressure and molar flow rates of the precursors. Typically, these reactions are carried out at temperatures between 1300°C and 1700°C and pressures between 0.1 and 200 torr. The molar flow rates are then adjusted to ensure stoichiometric B-N deposition. More recently, CVD with a single precursory compound containing both boron and nitrogen such as borazine(*29*), ammonia-borane(*30*) or borane-amine organocomplexes(*31*) has gained appeal. Benefits of single-precursor over double-precursor CVD are lower reaction temperatures and elimination of precursor flow rate ratio optimization. However, contamination (especially carbon and oxygen) becomes an issue with complex precursors.

The crystalline quality of pBN is less than desirable as the hBN layers exhibit stacking disorder.(*32*) Therefore, since single crystal (and especially bulk crystal) hBN is not possible with CVD, solution/precipitation methods have been investigated in the last few years. Many solvents have been tested for bulk cBN crystallization at high-pressure, high-temperature (HPHT) conditions including Fe-Al, Co, Co-Al and Ni-Al(*33*) as well as alkali and alkaline-earth metals(*34*). Taniguchi and Watanabe(*35*) used a barium boron nitride ($Ba_3B_2N_4$) solvent to dissolve hot-pressed BN and powder BN at 4-5 GPa and 1500-1650°C for 20-80 hours. Since these conditions are close to cBN/hBN phase equilibrium, a mixture of the two phases was produced. Crystal size appeared to be less than one millimeter across, and the sensitivity of alkali and alkaline-earth metal solvents to air and moisture were significant disadvantages of this solvent. Kubota and Watanabe(*36*) performed another HPHT synthesis of cBN/hBN with a Ni solvent at 4.5-6 GPa and 1300-1900°C for 20 minutes. These crystals ranged from 5 μm (cBN) to 25 μm (hBN) across. While the crystals were small, the nickel solvent proved more stable and easier to work with.

cBN synthesis requires high pressure as evidenced from the aforementioned studies. But since hBN is the predominant phase at low pressures, this suggests that it can be grown from similar cBN metal solvents at significantly lower pressures. One of the first attempts to grow

hBN single crystals was by Ishii and Sato(*37*) with boron dissolved in a silicon flux in a nitrogen atmosphere. After cooling from a temperature of 1850°C for two hours, their largest hBN crystal was reportedly two millimeters across and 20 μm thick. However, the hBN crystals were yellow in appearance due to carbon impurities and also contained nitrogen vacancies. Yang et al.(*38*) synthesized hBN by dissolving 0.5-μm cBN crystals in a layer of molten Ni under a H_2 and N_2 atmosphere at 30 torr and about 1300°C. The hBN crystals they produced were only 2 μm across, most likely because nitrogen solubility in molten nickel is small (<0.01 wt% at 1550°C and 1 atm).(*39*, *40*) Kubota et al.(*41*) dissolved BN powder in a nickel solvent that contained 40 wt% molybdenum to increase nitrogen solubility an order of magnitude over pure nickel;(*40*) the result was single hBN crystals that were 300 μm across and 10 μm thick. Their reported experimental conditions were 1350-1500°C for 12 hours followed by 4°C/hour cooling to 1200°C and quench cooling thereafter. Since chromium dissolves nitrogen up to two orders of magnitude better than molybdenum,(*40*, *42*) Kubota et al.(*43*) mixed 53 wt% chromium with the nickel solvent under the same aforementioned conditions and obtained hBN crystals 500 μm across and 60 μm thick.

This present work further explores the synthesis of bulk, single crystal hBN using primarily a nickel-chromium solvent as well as pure nickel and copper solvents. No Ni-Cr-B-N quaternary phase information exists, but many binary phase diagrams(*44–46*) and a ternary Ni-Cr-B phase diagram(*47*) are reported in literature. To take advantage of a wide temperature range and to incorporate as much nitrogen dissolution as possible, the eutectic point at 53 wt% chromium, 47 wt% nickel and 1345°C was the chosen Ni-Cr solvent composition for hBN precipitation from BN powder.

Bulk crystal growth from a boron powder source is appealing because boron powder enriched in ^{10}B is commercially available while ^{10}B-enriched BN powder is not. Since thermal neutrons only interact with boron-10, isotopic enrichment of bulk hBN crystals proves advantageous. So far, hBN bulk crystal growth has relied on cBN(*38*) or BN powder(*41*, *43*) source materials which contain boron in its natural abundance— about 80% ^{11}B and 20% ^{10}B. Therefore, synthesis of hBN from boron powder was tested with Ni-Cr, pure nickel, and pure copper solvents. The relative amounts of boron and metal powders used in each experiment were chosen from the eutectic point compositions of the solvent systems shown in Table 1-2.

Table 1-2 Eutectic information of Ni-Cr, Ni-Cr-B, Ni-B and Cu-B systems(*44–47*)**.**

Components	Composition (at. %)				Temperature (°C)
	Boron	Nickel	Chromium	Copper	
Ni-Cr		44	56		1345
Ni-Cr-B	18.3	65.6	16.1		1050
	35.6	49.7	14.7		1096
Ni-B	45	55			1018
Cu-B	13			87	1013

Chapter 2 - Experiments and Analytical Tools

This chapter describes the apparatus and procedures for two crystal growth methods followed by descriptions of analytical tools to characterize hBN crystals.

Crystal Growth

hBN single crystals were grown by two solution methods: I.) dissolution of boron nitride powder and subsequent precipitation of hBN employing a nickel-chromium solvent; II.) synthesis of hBN by dissolving boron in a metal solvent saturated with nitrogen, then slowly cooling to precipitate hBN.

I. BN powder recrystallized in nickel-chromium solvent

Boron nitride dissolution/precipitation experiments were carried out in three types of furnaces. A vertical resistively-heated graphite tube furnace (Figure 2-1) was used for most experiments. As purity became an issue, a similar furnace with tungsten resistive heating elements (Figure 2-2) was employed to reduce the potential for carbon contamination. Both furnaces, manufactured by Centorr Vacuum Industries, are water-cooled with maximum temperatures above 2000°C. They come equipped with both mechanical and diffusion vacuum pumps and a pyrometer temperature sensor. A programmable thermostat allowed for smooth control of set points and ramps. A third furnace manufactured by CM Furnaces was also used. This horizontal alumina tube furnace (Figure 2-3) with molybdenum disilicide heating elements and a maximum operating temperature of 1550°C was air-cooled and equipped with a programmable thermostat and mechanical vacuum pump. The temperature in the CM furnace was measured with Type R thermocouples. All three furnaces were rated for high-vacuum operation with a maximum operating pressure of 850 torr.

The source materials employed and their residual impurity concentrations are summarized in Table 2-1. Boron nitride powder, grade HCJ48 from the Advanced Ceramics Corp. with a specified purity of 0.220 wt% oxygen and 0.028 wt% carbon, was the BN source material. Two nickel powders were used, one supplied by Acros Organics at 99.9% purity, the other supplied by Alfa Aesar at 99.999% purity with carbon guaranteed < 100 ppm. Chromium pellets were supplied by Cerac/Materion Advanced Materials at 99.998% purity. Boron powder

manufactured by Materion at 99% purity was used in the hBN direct synthesis experiments. Nitrogen, argon and ammonia gases were supplied by Linweld/Matheson Trigas at 99.99% purity or greater.

Table 2-1 Source materials and their lot-certified impurity concentrations

Material	Source	Major impurities and concentrations		
BN powder (Grade HCJ48)	Advanced Ceramics Corp.	O: 0.220%	C: 0.028%	
Nickel powder, 99.998%	Alfa Aesar	Si: 3 ppm Mg: 1 ppm	Fe: 3 ppm C: 10 ppm	Ca: 1 ppm
Nickel powder, 99%	Acros Organics	C: 880 ppm	O: 1000 ppm	
Chromium powder, 99.998%	Materion	O: 0.0190% Si: <0.0004%	Fe: 0.0006% Pb: <0.0004%	Zn: <0.0005%
Boron powder, 99%	Materion	Si: 0.1% Fe: 0.08%	Mg: 0.09% Mn: 0.02%	Al: 0.08%
Nitrogen gas, ultra-high purity	Linweld/ Matheson Trigas	CO_2: <1 ppm H_2O: <1 ppm	CO: <1 ppm THC: <0.5 ppm	O_2: <1 ppm
Argon gas, ultra-high purity	Linweld/ Matheson Trigas	N_2: <4 ppm O_2: <1 ppm	CO_2: <1 ppm H_2O: <1 ppm	CO: <1 ppm
Ammonia gas, 99.99%	Linweld/ Matheson Trigas	CO_2: <10 ppm	O_2: <10 ppm	THC: <10 ppm

THC = total hydrocarbons

Two crucible materials were chosen to hold the reactants in the furnaces: hot-pressed boron nitride (HPBN) and pyrolytic BN (pBN). The benefit of using BN crucibles was minimal system contamination since crucible and source material are one-and-the-same, but the nickel-chromium solvent would dissolve portions of the walls. 12”-long, 1”-diameter HPBN rods available from Momentive Performance Materials were cut into 1 ¾”-tall, ¾”-inner diameter

crucibles which were durable and withstood repeated experiments. While pBN crucibles were less durable due to their extremely thin walls (~1 mm thick), they contained less impurities and were thus appealing in high-purity experiments.

Samples heated in the graphite and tungsten furnaces were contained in a hot-pressed boron nitride (HPBN) crucible inside a retort of appropriate material (graphite for graphite furnace, tungsten for tungsten furnace). BN powder was added to the crucible first, followed by nickel powder and chromium pellets. Before heating, the loaded furnace was cycled through three evacuation/N_2 purge steps, with the last evacuation at pressures between 10^{-5} and 10^{-6} torr, to remove as much oxygen, water and other volatile contaminants as possible from both the furnace chamber and the sample. Samples heated in the horizontal alumina tube furnace were contained in a pyrolytic boron nitride (pBN) boat loaded from bottom to top with BN powder, Ni powder and chromium pellets. Before heating, three cycles of evacuations and N_2 purges were performed, with the last evacuation being < 100 mTorr.

Optimum crystal growth conditions were sought by adjusting the temperature at which the sample was held for BN powder dissolution (i.e. soak temperature), the time held at the soak temperature (soak time), and the cooling rate from the soak temperature to solvent solidification. Soak temperatures ranged from 1450°C to 1725°C with soak times of 6-72 hours and cooling rates of 2-8°C/hr. Experiments were performed under a nitrogen ambient slightly over atmospheric pressure (830 to 850 torr) to prevent air from leaking into the system. hBN crystals were then separated from the metal solvent by one of two methods: if the crystals were loosely attached to the Ni-Cr, then they could be removed easily with forceps; if the crystals were strongly attached to the Ni-Cr, then the whole sample was immersed in hot aqua regia to dissolve away enough of the metal to separate the crystals.

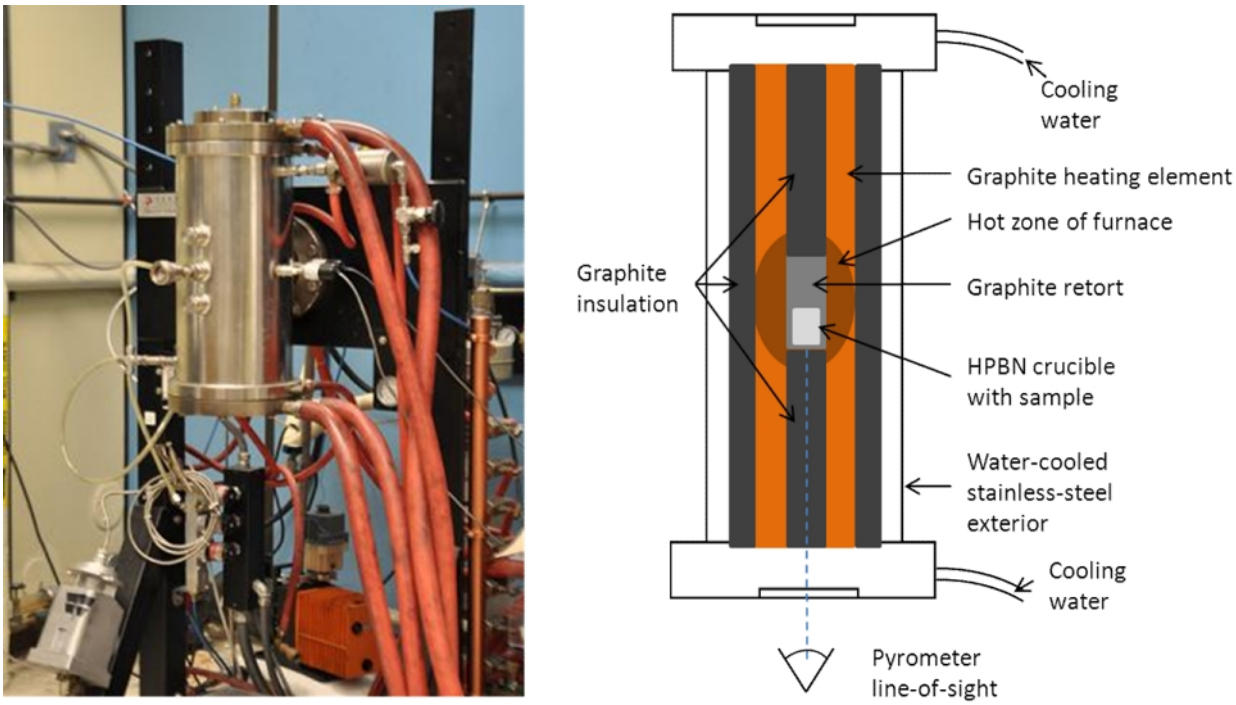

Figure 2-1 Photo (left) and schematic of internals (right) of the graphite resistive element furnace used for the majority of hBN crystal growth experiments with important features labeled. Vacuum and temperature control systems not pictured.

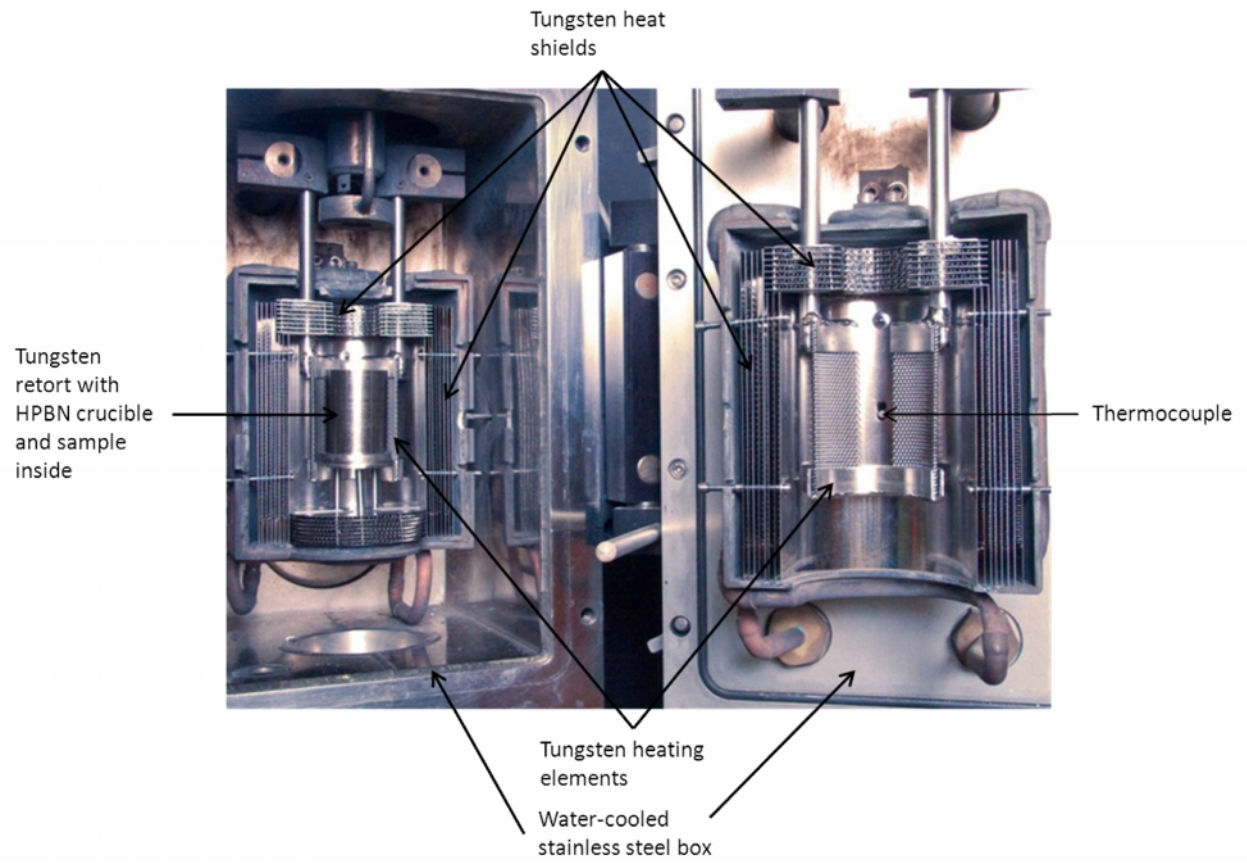

Figure 2-2 Photo of the interior of the tungsten resistive element furnace with important features labeled. Vacuum and temperature control systems not pictured.

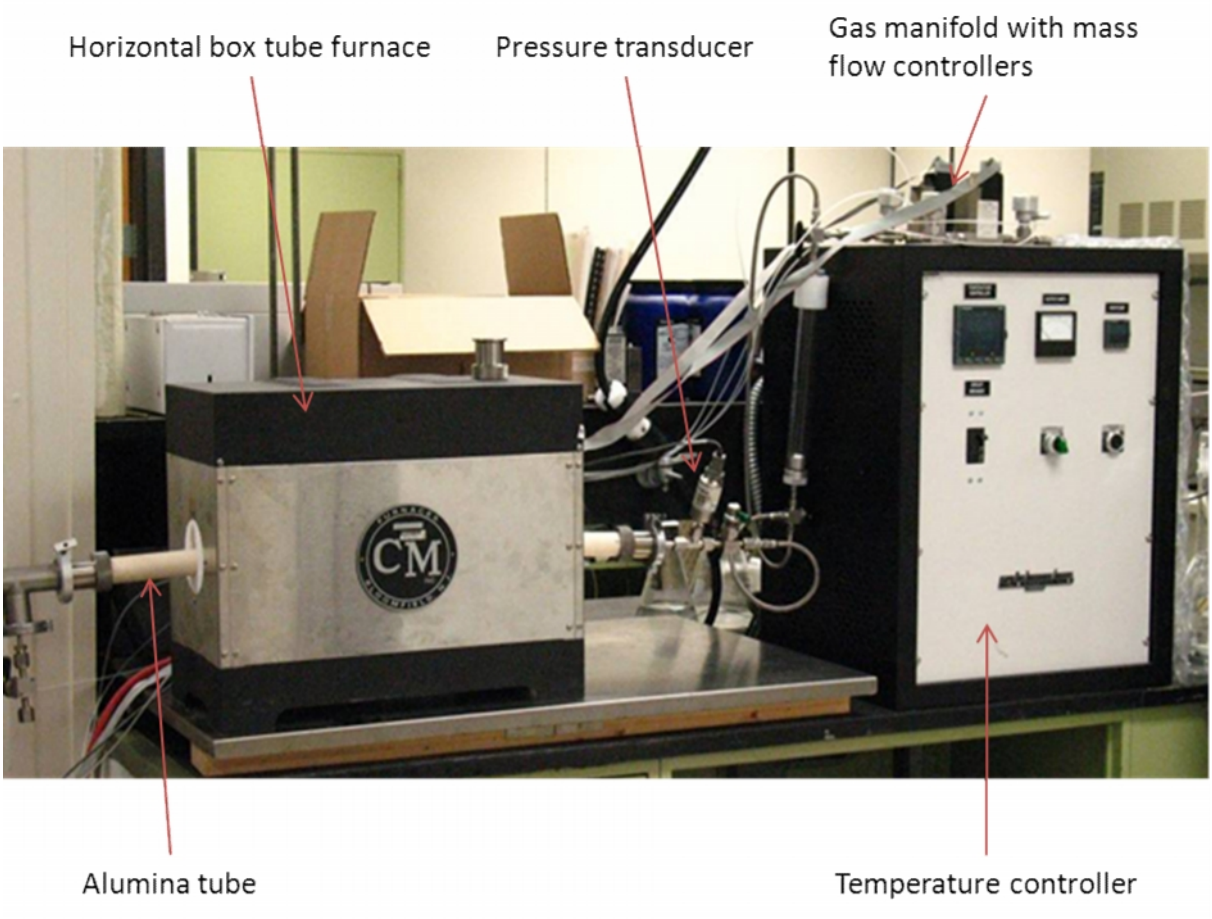

Figure 2-3 Photo of CM horizontal box tube furnace with important features labeled. Vacuum and pressure control systems not pictured.

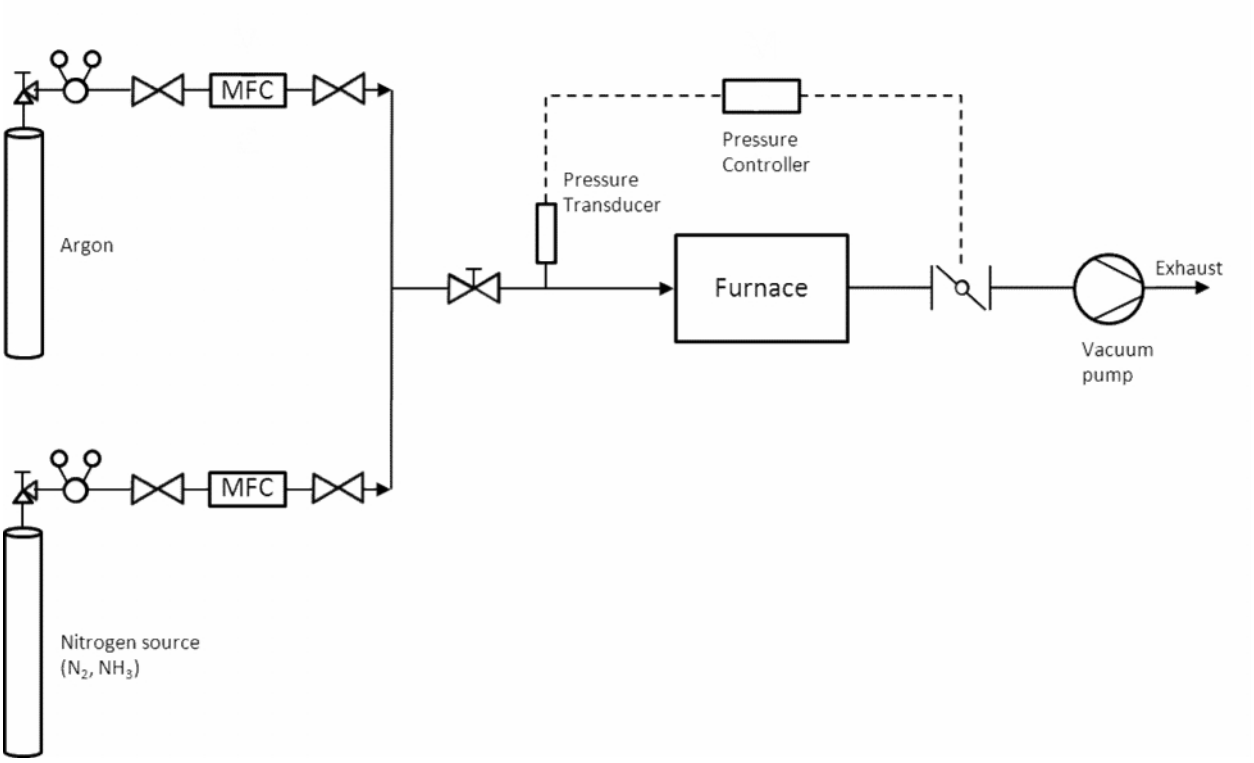

Figure 2-4 Schematic of CM furnace system with gas manifold and pressure control.

II. Direct synthesis from boron powder and nitrogen compound in metal solvent

hBN synthesis from boron powder was performed in the (horizontal tube) CM furnace shown in Figure 2-3 and Figure 2-4. The solvents tested were pure nickel, nickel-chromium, and pure copper. Boron powder was mixed with the metal powder, loaded into a pBN boat and placed in the alumina tube of the furnace. Before heating, three cycles of evacuations and argon purges were performed, with all three evacuations being < 100 mTorr. The chamber was then backfilled with the chosen nitrogen source (nitrogen gas or ammonia) to a pressure slightly above atmospheric (780 to 800 torr) and heated at 1200-1550°C for 3-12 hours then cooled at 4-8°C/hr until solvent solidification. Continuous gas flow was provided by a gas manifold with mass flow controllers and the pressure regulated by a butterfly valve with pressure controller. Following the experiment, synthesized crystals were removed from the solvent using forceps.

Methods of hBN Characterization

Several methods were utilized to verify hBN identity and crystal quality. Analytical tools included scanning electron microscopy coupled with energy-dispersive x-ray spectroscopy, x-ray diffraction, Raman microscopy, photoluminescence spectroscopy, transmission electron

microscopy and differential scanning calorimetry. For a qualitative analysis of defects in the crystal structure, defect-selective etching was performed.

Scanning Electron Microscopy (SEM) and Energy-Dispersive X-ray Spectroscopy (EDS)

Scanning electron microscopy (SEM) is a form of high-resolution microscopy that generates an image of a sample by directing a beam of electrons towards a sample and analyzing the emitted electrons from the sample.(*48*) SEM has superior resolution than optical microscopy and more information can be extracted from emitted electrons (elemental composition, fine topography, etc.) than reflected light. Electrons scattered by the sample are primarily one of two types: secondary electrons or backscattered electrons. Secondary electrons are useful for fine topographical imaging of the sample surface while backscattered electrons scatter in proportion to an atom's atomic number, thus providing contrast among light and heavy atoms in the sample image. A schema of important SEM features is presented in Figure 2-5.

By consequence of a high-energy electron beam directed on the sample, electrons from the inner shells of atoms can be ejected.(*48*) When an electron from outer (high energy) shells replaces the electron ejected from the inner (low energy) shell, the energy that the outer-shell electron must lose going to the inner shell is emitted as a characteristic X-ray. The X-ray energy is unique to the element and thus can be measured by energy-dispersive X-ray spectrometry (EDS) to determine the type and abundance of elements in the sample.

The SEM system employed in this study was a FEI Nova NanoSEM 430 with Oxford X-Max Large Area Analytical EDS silicon drift detector (SDD) (80mm^2). Typical accelerating voltages range from 1-30 kV, and the highest resolution achievable is 0.8 nm at 30 kV. Standard detectors include the Everhart-Thornley detector (ETD) and Through Lens detector (TLD), but the high-vacuum environment required by these detectors is not always suitable for imaging hBN. Since hBN is electrically insulating, electric charges due to continuous electron bombardment accumulate on the surface, thus distorting the image captured by these detectors. An alternative is to coat the sample surface with a metal by sputtering, but this could potentially distort the surface topography. Therefore, the low voltage high contrast detector (vCD) and low vacuum detector (LVD) became invaluable because the hBN sample could be analyzed at low vacuum with a small amount of water vapor to dissipate charging effects.

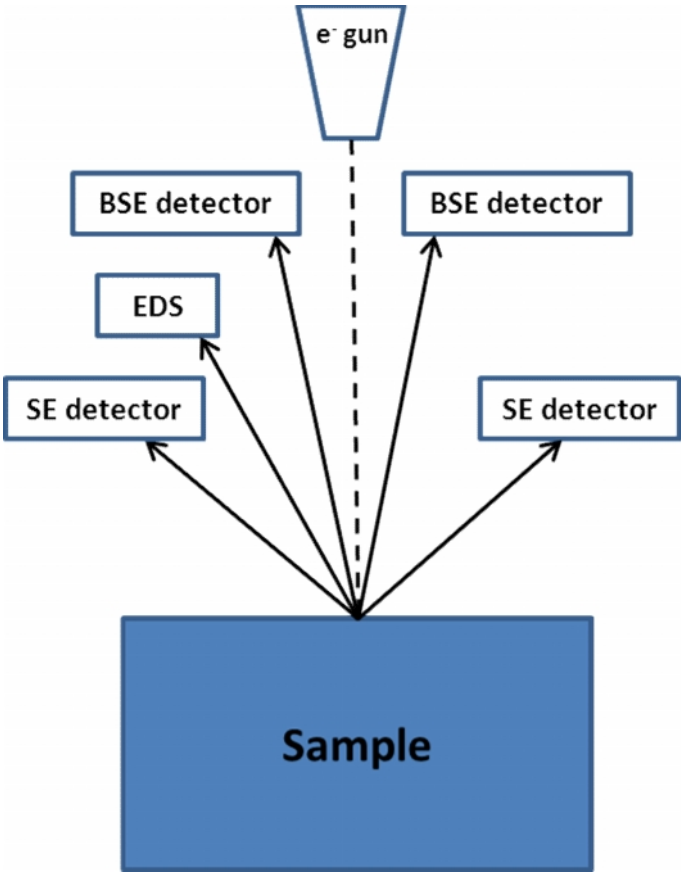

Figure 2-5 Schema of typical SEM operation.

X-ray Diffraction (XRD)

X-ray diffraction (XRD) is a nondestructive technique to investigate the structure of solids.(*49*) The technique is predicated on wave interactions with matter. When incident on a crystal lattice at some angle θ, x-rays reflect off individual atoms from different atomic planes; constructive interference occurs when the extra distance they travel between planes is an integer-multiple of the wavelength, resulting in a high x-ray intensity that appears as a peak in the XRD spectrum. The angle, θ, when this constructive interference occurs along with the x-ray wavelength λ and spacing *d* between the planes of atoms are related by Bragg's law, $n\lambda = 2d\sin\theta$; see Figure 2-6. *n* is the order of the diffraction, but it is typically grouped with *d* in reported *d*-spacings (i.e. for hBN, *d*(001) = 0.666 nm, *d*(002) = ½ *d*(001) = 0.333 nm, etc.). Therefore, by adjusting the angle between the sample and an x-ray source of known wavelength, the angles that produce peaks in the XRD spectrum correspond to ordered planes of material with atomic spacing *d* calculated by Bragg's law.

XRD spectra in this study were collected using a Rigaku MiniFlex II powder x-ray diffractometer with a Cu Kα x-ray source (λ = 0.154056 nm). Raw spectral data were then analyzed by PDXL x-ray diffraction software to identify diffraction peaks and match to ICDD PDF card data.

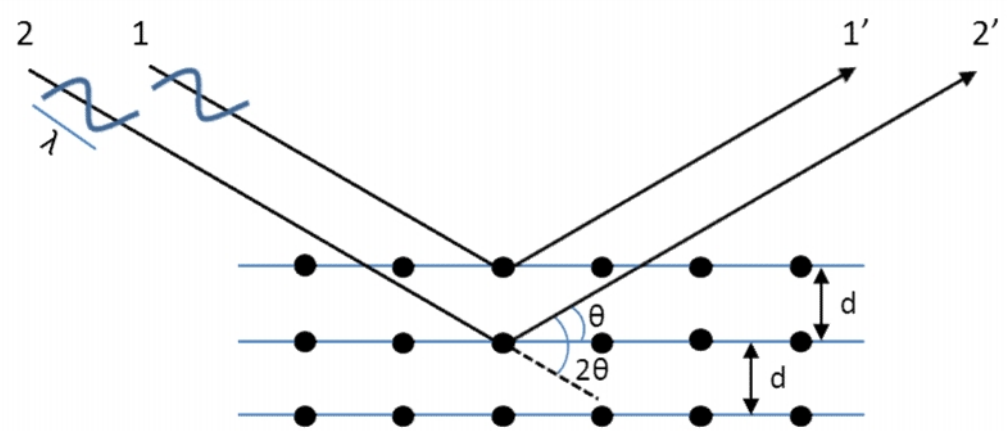

Figure 2-6 Depiction of x-ray interaction with crystalline planes of atoms. Parameters that appear in Bragg's law are indicated.

Transmission Electron Microscopy (TEM) and Selected Area Electron Diffraction (SAED)

Transmission electron microscopy (TEM) is similar to SEM with the exception being that the sample image is generated from electrons that are scattered passing through the sample instead of reflecting off of the sample.(*48*) Consequently, samples analyzed by TEM must be thinner than those analyzed by SEM to permit electron transmission. A schema of TEM is shown in Figure 2-7. While SEM generates images of the sample surface, TEM can illuminate structural features within the sample such as defects. This makes TEM incredibly useful for structural characterizations of defects such as edge and screw dislocations since they can be directly imaged. Along with sample imaging, the system is capable of selected area electron diffraction (SAED).(*49*) The principles of SAED are the same as those of XRD, except electrons are scattered instead of x-rays. This allows for a much smaller sampling area and greater atomic detail in the pattern. The resulting pattern of spots is the selected area diffraction pattern (SADP) and represents the crystal structure in terms of the reciprocal lattice.

TEM images in this study were taken using a JEOL JEM 2100 Transmission Electron Microscope courtesy of Dr. Karthik Chinnathambi at Boise State University. Typical

accelerating voltages ranged from 80-200 kV. Magnification up to 1,500,000x is possible with a resolution of 0.14 nm. Samples of bulk hBN were prepared for analysis by mechanically peeling thin layers of material from bulk hBN crystals.

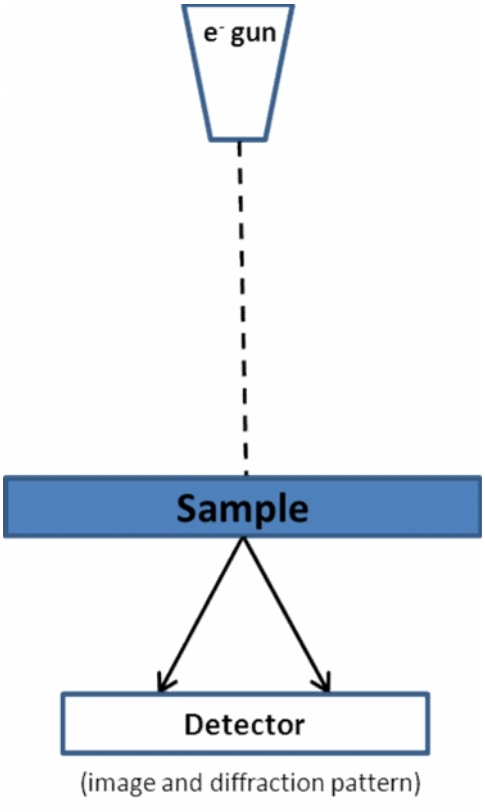

Figure 2-7 Schema of TEM operation.

Raman Microscopy

Raman microscopy is a form of vibrational spectroscopy that yields information on the types of chemical bonds present in the sample. Light incident on a solid sample is mostly reflected without a change in frequency, ν_0, but a small amount of light is scattered at a different frequency, $\nu_0 \pm \nu$.(*50*) The change in frequency ν is due to Raman scattering and is characteristic of vibrational modes in the solid. This Raman shift in frequency is only seen when the incident light induces a change in polarizability of the solid. Thus, not all vibrational modes are Raman active. Since every type of molecule has unique chemical bonding environments, Raman spectra are unique to every compound and can be used to identify the sample and the structure of the material. For example, Raman spectroscopy can be used to distinguish hBN from cBN. However, materials with molecular similarities are difficult to distinguish such as hBN and rBN.

The width of the Raman peak, typically measured by the full-width half-maximum (FWHM), is a measure of the crystal quality and uniformity. Defects in the solid cause nearby bonds to be stretched or compressed, leading to a range of Raman shift frequencies. A narrow peak (i.e., small FWHM) indicates a well-ordered crystal with minimal defects.

Raman spectra were obtained using a LabRAM ARAMIS Raman spectrometer at the University of Kansas Bioengineering Research Center with a HeNe laser (633 nm, laser power of 17 mW). Table 2-2 summarizes some Raman data collected on hBN of various crystalline qualities. A Raman shift of 1366 cm^{-1} is widely reported as the fundamental E_{2g} vibrational mode and is the only observable Raman-active mode in hBN.

Table 2-2 Raman data on hBN from selected sources.

Peak Position, cm^{-1}	*FWHM, cm^{-1}*	*Sample*	*Reference*
1365	9.1	Single crystal	(*41*)
1366	20	Single crystal	(*51*)
	---	Powder	(*52*)
	31	CVD/Epitaxy	(*53*)
	---	Single crystal	(*38*)
1367	9	Single crystal	(*43*)
1370	15	Powder	(*54*)

Photoluminescence Spectroscopy (PL)

Photoluminescence spectroscopy (PL) is a nondestructive optical technique by which energy states within a material can be measured. For intrinsic semiconductors, the energy of an emitted photon is characteristic of the energy necessary for an electron to jump from the valence band to the conduction band. Electrons are forbidden to acquire energy that would put them in between the valence and conduction bands (i.e. within the band gap). However, allowed energy states within the band gap can be introduced by impurities or defects within the semiconductor. Thus, PL spectra are qualitatively useful for determining purity and structural quality of a semiconductor material.

In this study, PL spectra were obtained at a temperature of 300K by a deep UV laser spectroscopy system consisting of a Ti/sapphire laser with an excitation energy ~6.2 eV courtesy of Dr. Hongxing Jiang and Dr. Jingyu Lin of the Texas Tech University Nanophotonics Center. Table 2-3 presents some luminescence data taken on hBN from several authors. The band gap of hBN remains in dispute, but recent reports seem to be converging close to 6 eV. Subsidiary bands in the PL spectra often occur and are usually explained as bound-exciton luminescence from stacking faults or lattice plane shearing(*7*), Frenkel excitons(*55*), and donor-acceptor pair recombinations(*56*). Watanabe and Taniguchi(*55*) have an extensive report on the bands that appear in room temperature and cryogenic PL spectra of hBN in which they introduce the Jahn-Teller effect to harmonize experimental results with theoretical calculations. Cryogenic PL is advantageous because the peaks are sharper and certain impurity-related transitions are suppressed.

Table 2-3 Luminescence data on hBN from selected sources.

Luminescence type	**Temp. (K)**	**Band gap (eV)**	**Subsidiary spectral peaks (eV)**	**Sample**	**Ref**
PL	N/A	5.82	4.52, 4.44 (*Frenkel excitons*)	Powder	(*57*)
PL	300	5.28	4.71 *(defect level)*	Film	(*56*)
PL	10	6.4*	5.48, 5.5, 5.57, 5.64 *(bound-exciton)* 5.32 *(donor-acceptor recombination)*	Single crystal	(*7*)
PL	8	N/A	5.4-5.7 *(stacking faults)* 5.8-5.928 *(stacking faults)*	Single crystal	(*55*)
CL	83	5.971	5.8-5.96 *(impurity or dislocation)* ~4.0 *(vacancies, carbon or oxygen impurities)*	Single crystal	(*6*)

PL = Photoluminescence CL = Cathodoluminescence

* measured from photoconductivity analysis coupled with photoluminescence

Differential Scanning Calorimetry (DSC)

Differential Scanning Calorimetry (DSC) is a technique to measure material phase properties, such as the temperature at which a substance melts and the heat capacity of a substance. A DSC system consists of two cells, a sample cell and a reference cell as shown in

Figure 2-8. Care must be taken to choose a reference sample that does not undergo a phase change at the conditions investigated (commonly a ceramic material like alumina is chosen). Both cells are heated by separate heating elements with their temperatures and required heat fluxes measured separately. The analysis begins by ramping the heat to both cells in a controlled manner so as to keep their temperatures equal. As the melting point of the sample is reached, the heat flux to the sample dramatically increases compared to the heat flux to the reference cell in an attempt to keep the temperature the same in both cells. The resulting spike in the DSC profile corresponds to the sample melting temperature. When the direction is reversed (cooling instead of heating the sample), a similar event occurs where the heat flux to the sample is dramatically decreased compared to the heat flux to the reference cell. This inverse spike in the DSC profile corresponds to the sample freezing temperature. Ideally, these melting and freezing peaks should occur at the same temperature, but often in multicomponent and multiphase systems, the peaks have a slight offset in temperature due to kinetic effects.

DSC data from residual metal solutions in this study were collected from a Perkin-Elmer Pyris I Differential Scanning Calorimeter (DSC) courtesy of the Ames Laboratory at Iowa State University. The standard cell and sample crucible were both high-fired alumina.

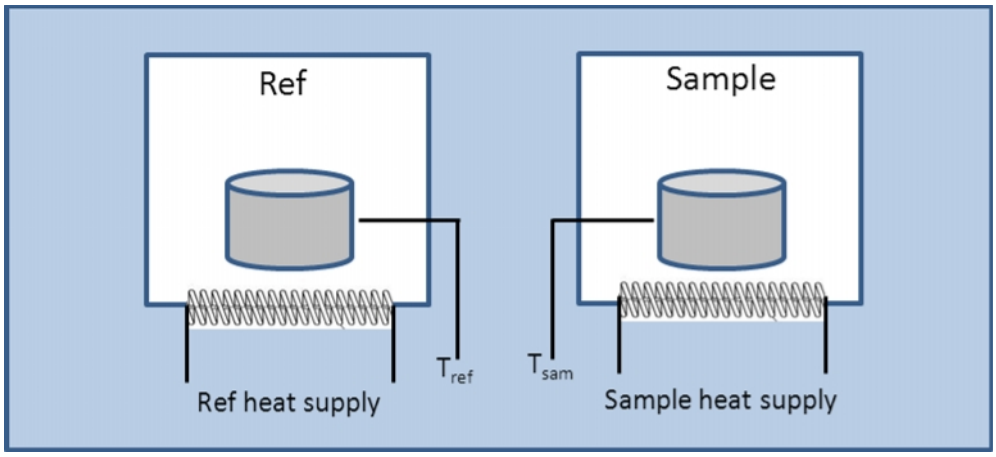

Figure 2-8 Schematic of typical differential scanning calorimeter.

Defect-Selective Etching

Defect-selective etching (DSE) is a common method to assess the general quality of a single crystal or epitaxial layer. The crystal is more reactive where impurities or defects are located. Thus, with proper etchant and etch conditions (temperature and time), these defects can be revealed by the presence of etch pits. The number of etch pits per square centimeter of crystal

plane area is known as the etch pit density (EPD) and is a useful measure of crystal quality. In addition, the shape and size of the etch pits can be correlated with the type of defect by calibration with other techniques such as TEM or x-ray topography.

Molten alkali (frequently potassium hydroxide) is one of few materials that will react with hBN, and the aggressiveness of the reaction depends mainly on temperature and time. However, the etch must be selective in that it preferentially attacks defects and not all crystal surfaces equally. Therefore, experiments were undertaken to determine the proper etchant composition, temperature and time to uncover defects in hBN.

There are few, if any, etching studies of hBN in the literature. Filonenko and Mishina(*58*) etched cBN in KOH at 380°C in increments of one-half, one, two, and four hours. A study by Harris et al.(*59*) attempted to preferentially etch away hBN while depositing CVD cBN. They found an etchant of 1% CH_4 in H_2 to be effective and also discovered that hBN etches much faster than cBN. Patel and Bahl(*60*) studied etching in graphite, a similar two-dimensional material to hBN, and determined molten sodium peroxide at 380°C for 10 minutes uncovered screw dislocations.

In this study, a eutectic mixture of KOH and NaOH (~50 mol% each) with a melting temperature of 170°C was used as an etchant. KOH/NaOH is a common etchant for DSE on many semiconductor materials(*58*, *61–64*) because the melting point of pure KOH (406°C) can be too high for the range of optimum etching temperatures. The etchant was placed in a vitreous carbon crucible and brought to temperature by a resistively-heated canister furnace with external power supply. The crucible was placed on a ceramic block inside the furnace, and a Type K thermocouple measured the temperature of the block immediately beside the crucible. Temperatures of 300-550°C (±10°C) and times of 0.5 to 1.5 minutes (±10 sec) were explored. The results, including etch pit sizes, shapes, and densities, were characterized by optical and electron microscopy.

Chapter 3 - Results and Discussion

This chapter begins with the results of hBN crystal growth from a Ni-Cr-BN system along with some characterizations that support the composition and quality of the hBN crystals. Next, the results of a new method that directly synthesizes hBN crystals from boron powder and a nitrogen source are reported. Finally, an assessment of the structural quality of the bulk hBN crystals determined by chemical etching and TEM studies is provided.

hBN synthesis from BN powder recrystallized in nickel-chromium solvent

hBN has been reportedly grown to sizes of 500 μm using a nickel-chromium solvent and BN powder.(*43*) Following the procedure described in that study, additional experiments were carried out to increase the size sufficiently enough for useful characterization and implementation of the hBN crystals as neutron detector devices. After synthesis, several analytical methods were employed to characterize the bulk hBN crystals, including XRD, SEM/EDS, Raman spectroscopy, and photoluminescence.

Growth conditions and observations

Several experiments were performed to test the effects of soak temperature on hBN crystal size. The results of the most meaningful experiments are shown in Figure 3-1. A general trend in the data shows that increasing temperature yields wider crystals. On qualitative grounds, this makes sense as higher temperatures favor fewer nucleation sites as well as higher rates of diffusion of material to the crystallization site. Generally, these two processes begin to compete with one another at a high enough temperature, at which crystal size begins to decrease with increasing temperature.(*65*) Figure 3-1 does not display this type of behavior, insinuating that the optimum temperature may never have been reached. But due to increased metal volatilization and temperature limits of the reactor, soak temperatures above 1700°C were not attempted.

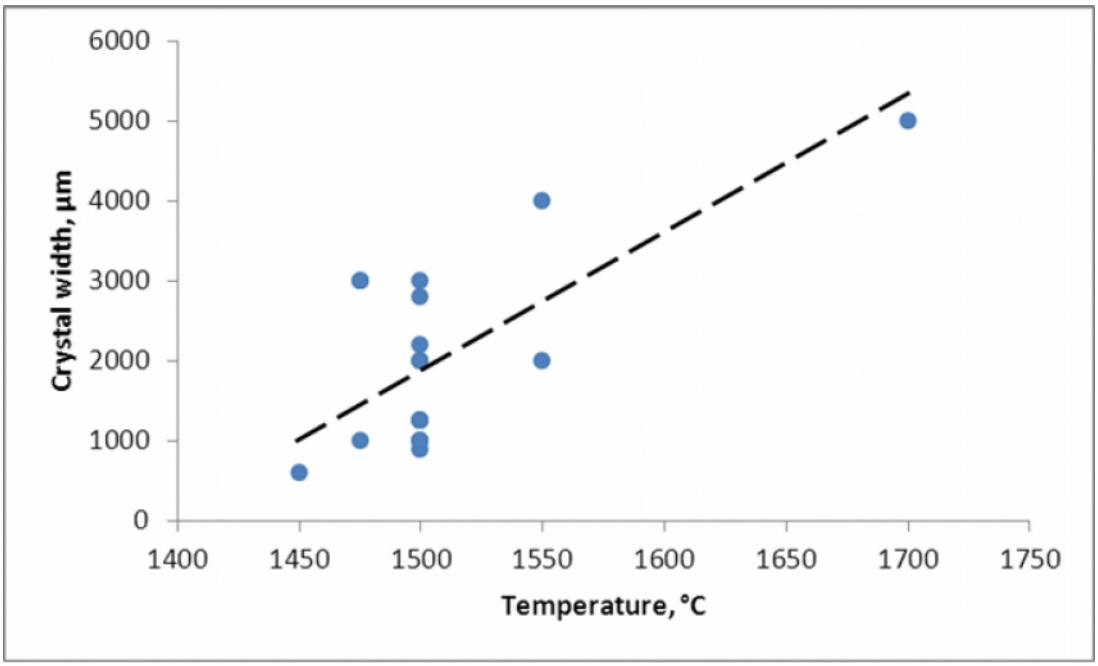

Figure 3-1 hBN crystal width (±100 µm) at various soak temperatures (±10°C). The dashed line highlights the data trend and has no theoretical basis.

Figure 3-2 shows images of hBN crystals synthesized with progressively higher soak temperatures. Three observations are worth noting from this figure: As the soak temperature increases, 1.) the width of crystals increases; 2.) the thickness of crystals decreases; and 3.) the shape of the crystals undergoes a fundamental change. The soak temperature affects the growth of the crystal in directions both parallel (a-direction) and perpendicular (c-direction) to the hexagonal planes of hBN as well as the growth rates of specific hexagonal planes. For instance, at a low soak temperature of 1475°C, growth is favored in the c-direction with uniform growth in the a-direction. Increasing the soak temperature increases growth in the a-direction seemingly at the expense of growth in the c-direction. Not only does lateral growth increase, but three of the six hexagonal sides grow faster than the others, changing the overall shape of the crystal from hexagonal to triangular. This phenomenon is illustrated in Figure 3-3. The reason for the large differences in "growth velocities" among the lateral planes is presently unknown but perhaps could be due to a stabilizing effect when crystal edges preferentially terminate with boron or nitrogen atoms as noted by Kim et al.(*30*) with thin-layered hBN.

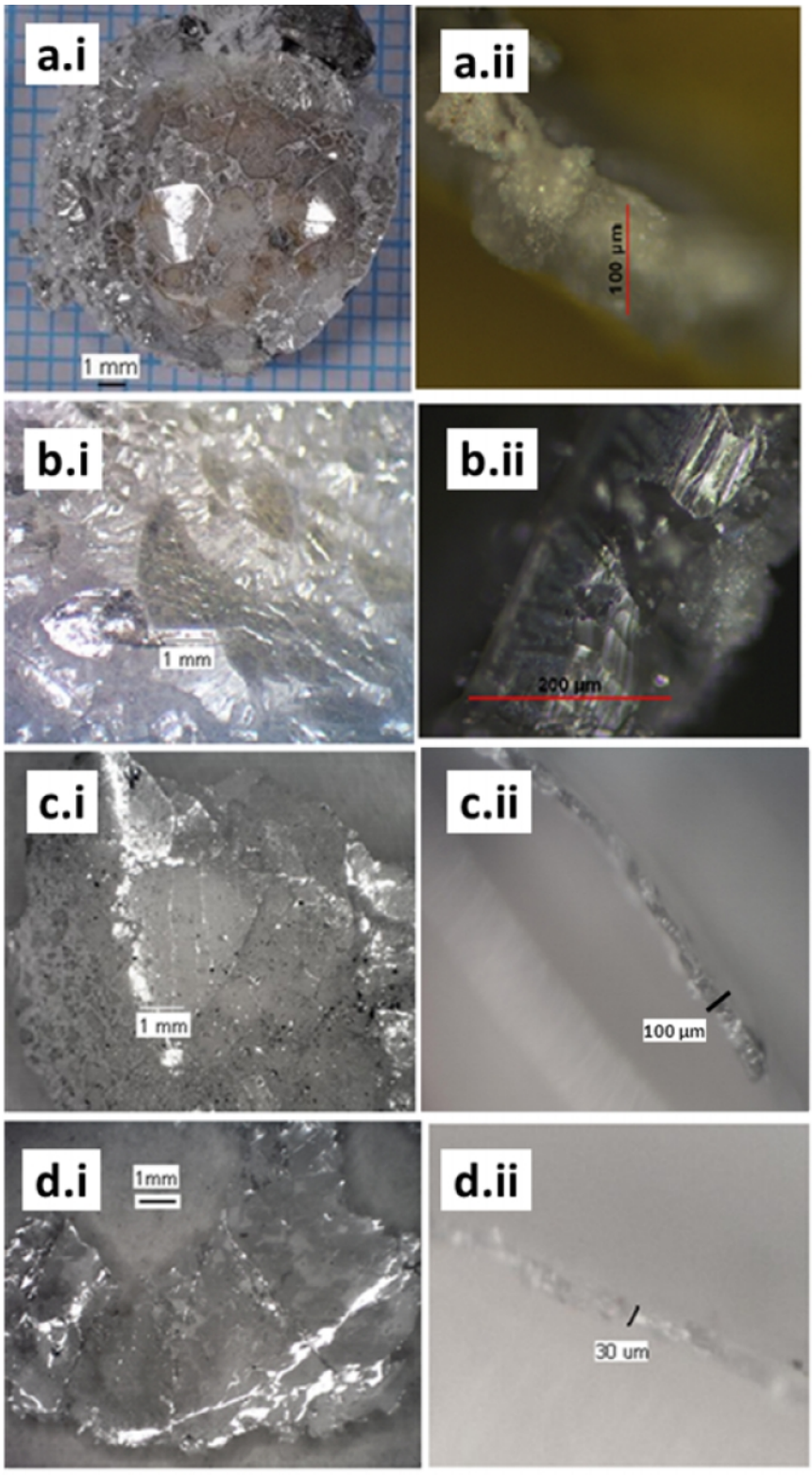

Figure 3-2 Width (i) and thickness (ii) of hBN crystals grown under soak temperatures of a) 1475°C b) 1500°C c) 1550°C and d) 1700°C.

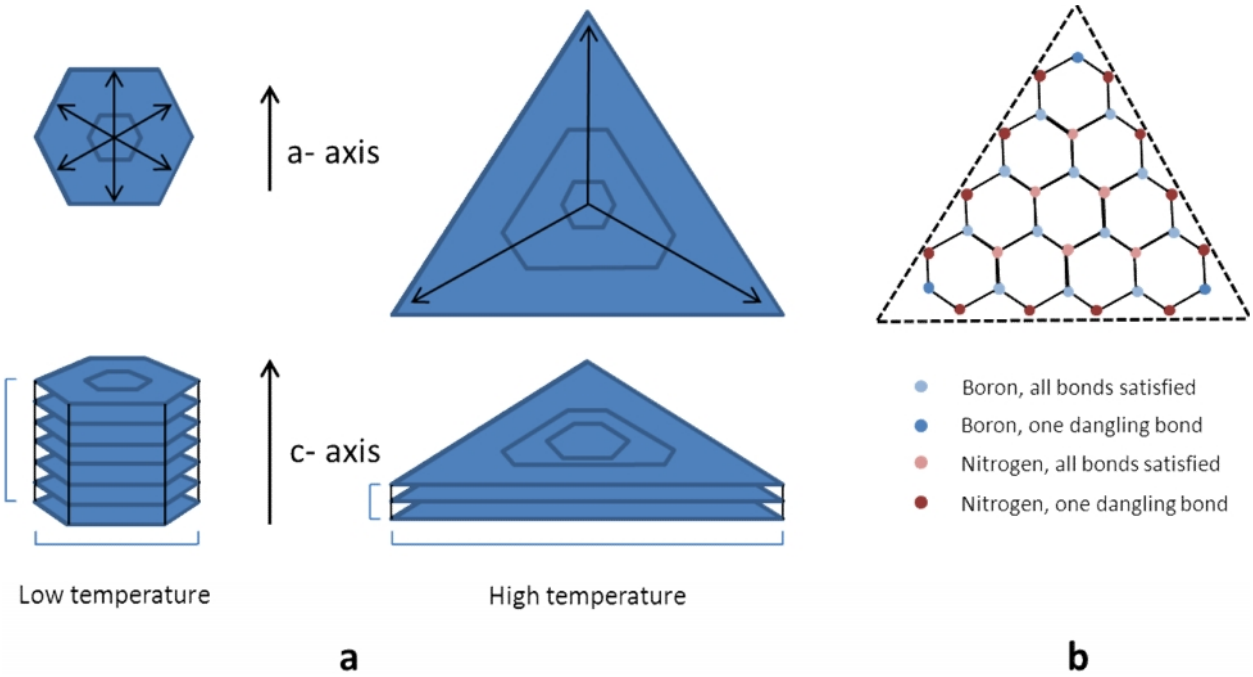

Figure 3-3 a) Illustration of relative growth rate and velocities of hBN crystals observed under low and high soak temperatures. Low temperatures promote growth in the c-direction and uniform growth in the a-direction. At high temperatures, growth is favored in three faces of the a-direction. b) Speculative chemical environment of triangular hBN crystal adapted from Kim et al.(*30*) **Edges containing atoms with dangling bonds may prefer one atom (nitrogen in this figure) over the other.**

The surface tension of liquid Ni-Cr solvent caused the hBN crystals to grow in a rounded shape as seen in Figure 3-4. This curvature likely induces strain in the crystals and could limit the size of their outward growth. A strange Ni-Cr "pan-handle" formed during many experiments, as seen on the left side of Figure 3-4. Perhaps as the experiment went into the cooling phase, the Ni-Cr sample froze from the surface inward, contracting at the surface enough to dispel molten metal through a weak spot and solidified as the pan-handle feature.

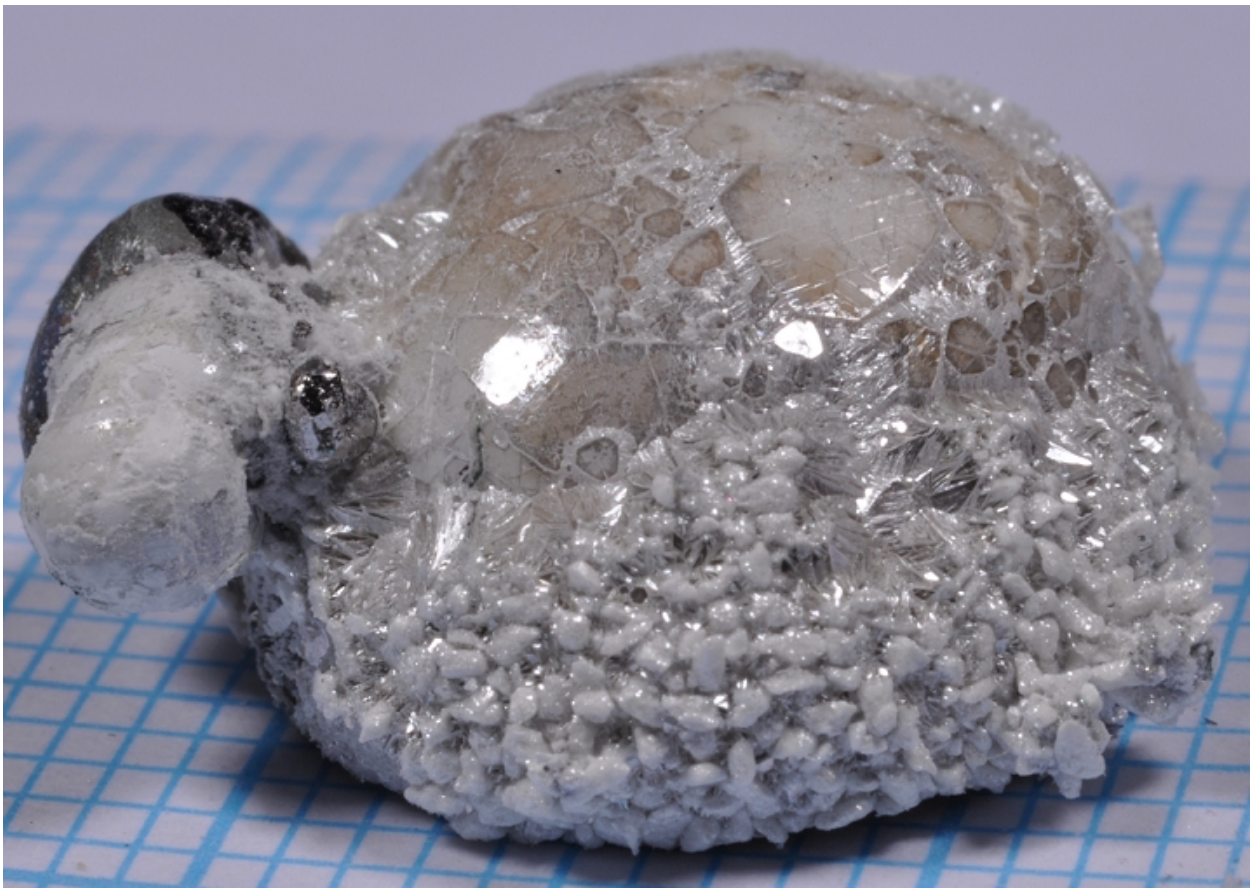

Figure 3-4 Typical post-experiment sample with hBN crystals covering the solidified Ni-Cr solvent.

As no Ni-Cr-B-N quaternary phase diagram is available, exact melting and solidification temperatures were unknown prior to this work. The Ni-Cr eutectic point of 1345°C and 53 wt% Cr made this system an appealing choice for a solvent because the ratios of the boron-dissolving nickel and nitrogen-dissolving chromium were comparable, giving us the best chance of dissolving both boron and nitrogen in amounts great enough for subsequent hBN precipitation. When heating the Ni-Cr-B-N system, the melting temperature was not a concern because it was sure to be below the Ni-Cr eutectic temperature of 1345°C since additional components tend to depress the initial melting temperature. However, the freezing temperature was important to know as it provides the lower temperature limit for crystal growth (the temperature at which we can expect crystal growth to be complete). Therefore, some samples of eutectic nickel-chromium that were previously used in hBN precipitation experiments were tested with differential scanning calorimetry (DSC) to determine the freezing point. Figure 3-5 is a DSC plot for such a sample and displays a freezing range between 1175°C and 1215°C. Therefore,

the freezing point of the system, and thus the cut-off temperature for crystal growth, has been lowered nearly 150°C from the initial Ni-Cr binary eutectic temperature.

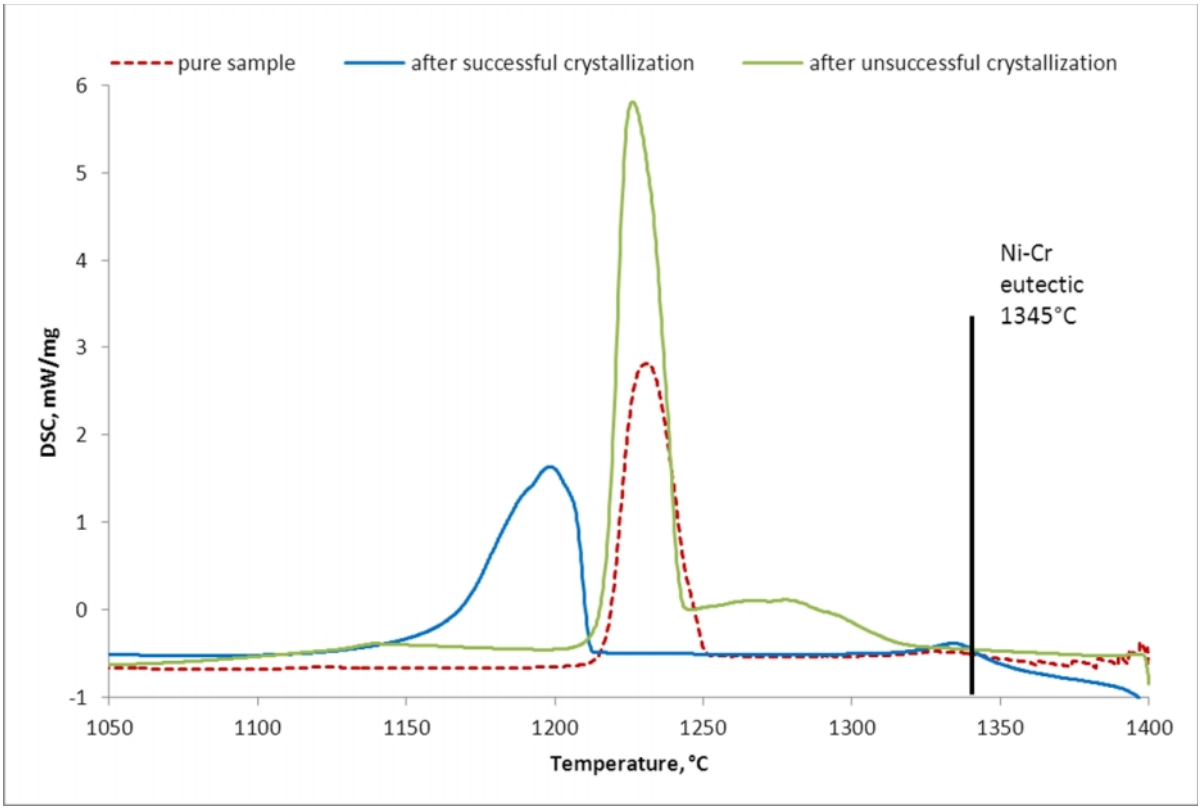

Figure 3-5 DSC freezing-segment data for three samples of nickel-chromium solvent: a pure sample not used in hBN crystallization; a sample after a successful experiment yielding hBN; and a sample that did not yield significant hBN

During the course of experiments, conditions with proven crystal growth results (i.e. 1500°C for 24 hours cooled at 4°C/hr) did not always yield large crystals. In some of these experiments, very little boron nitride powder dissolved in the Ni-Cr. The DSC plot in Figure 3-5 alludes to this since "pure" Ni-Cr and the Ni-Cr-B-N sample from an unsuccessful experiment had a similar freezing range that was about 50°C higher than the Ni-Cr-B-N sample from a successful experiment. Note that the "pure" Ni-Cr sample melted at a temperature lower than the eutectic temperature of 1345°C. The sample likely had small amounts of boron and nitrogen impurities as it was melted in a HPBN crucible.

Efforts to explain the lack of BN powder dissolution (and low reproducibility among experiments in general) could not be answered definitively. One possible explanation is poor

mixing among the molten Ni-Cr and the BN powder leading to a small surface/contact area for BN powder dissolution. The relatively high surface tension of nickel causes the Ni-Cr to bead instead of spreading out evenly to cover the BN powder and maximize contact area. A simple solution was to add more nickel and chromium to the crucible to promote an even distribution of Ni-Cr. But this caused the Ni-Cr to attack the walls of the HPBN crucible, thus embedding the Ni-Cr into the crucible with no hope of recovery without destroying the expensive crucible.

Poor process reproducibility may also be due to oxygen contamination from the HPBN crucible which contains traces of boric oxide as a binding agent. Alumina crucibles were tested as substitutes for HPBN crucibles for a few experiments, but no BN powder dissolved. The aluminum and/or oxygen from the alumina may have interfered with the experiment, however the concentrations of elements were below the EDS detection limits.

Only a few experiments were carried out to test the effects of soak time and cooling rate as these parameters impacted the length of the experiment considerably more than testing the soak temperature. Instances of power failure in the middle of an experiment, where the sample was essentially quench cooled from the soak temperature to ambient, yielded no discernible crystals. From this, it was concluded that the cooling rates have to be slow to precipitate quality crystals. Cooling at 4°C/hr was an appropriate rate. The soak temperature had a more pronounced effect on crystal size than the soak time. This seems reasonable if most crystal growth occurs during the cooling stage of the sample. Soak time only becomes a concern if it is not long enough for the solvent to saturate with boron and nitrogen. But since saturation is dependent on temperature, appropriate soak times are coupled with soak temperature, making comparisons across temperatures impractical. For instance, Figure 3-6 shows crystal sizes for different soak times with a fairly constant soak temperature ranging from 1500-1550°C; the optimum soak time appears to be around 24 hours for producing wide crystals at this soak temperature. However, the largest hBN crystals were synthesized by a soaking at 1700°C for only six hours.

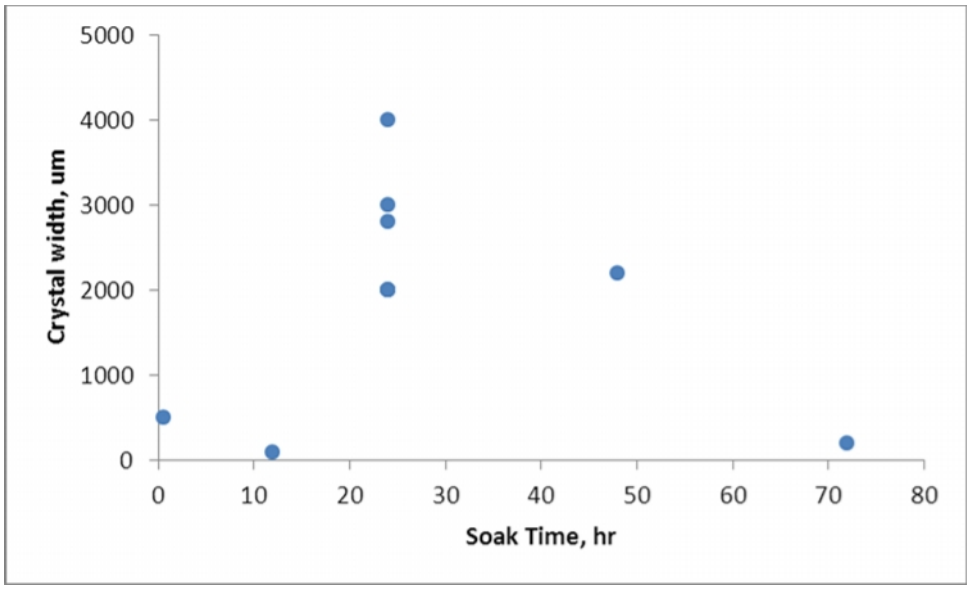

Figure 3-6 Crystal width versus soak time with soak temperature kept relatively constant at 1500-1550°C.

Characterizations of hBN

The hBN crystal quality and composition were characterized by multiple methods. The structure of the hBN synthesized from BN powder in Ni-Cr solvent was easily determined by XRD and Figure 3-7 shows XRD spectra for hBN crystals precipitated at 1550°C and 1700°C. The stacking planes along the c-axis [(002), (004), and (006)] dominate the spectra as expected. A few satellite peaks appear [(121), (131), etc.] possibly due to the polycrystalline material surrounding the single crystal being analyzed. Note the FWHM of the (002) peak for these two soak temperatures: the FWHM from the (002) plane decreases from 0.6° to 0.31° as the temperature increases from 1500°C to 1700°C. Thus the hBN precipitated at higher soak temperatures tends to be more ordered than those at lower soak temperatures.

Figure 3-8 shows an SEM image of small hBN crystals. EDS confirmed that this and other hBN samples contained boron and nitrogen in 1:1 atomic ratios. In some samples, a small amount of oxygen (<3%) was also detected possibly due to adsorbed water vapor or a thin native oxide layer. EDS of hBN under TEM also confirmed 1:1 stoichiometry and detected no impurities.

A Raman spectrum from an hBN crystal precipitated at 1450°C (Figure 3-9) exhibits a single peak at 1366 cm^{-1} in good agreement with many sources(*38, 51–53*). The FWHM of 8.0

cm^{-1} is one of the narrowest reported in literature to date, signifying excellent crystal structure quality.

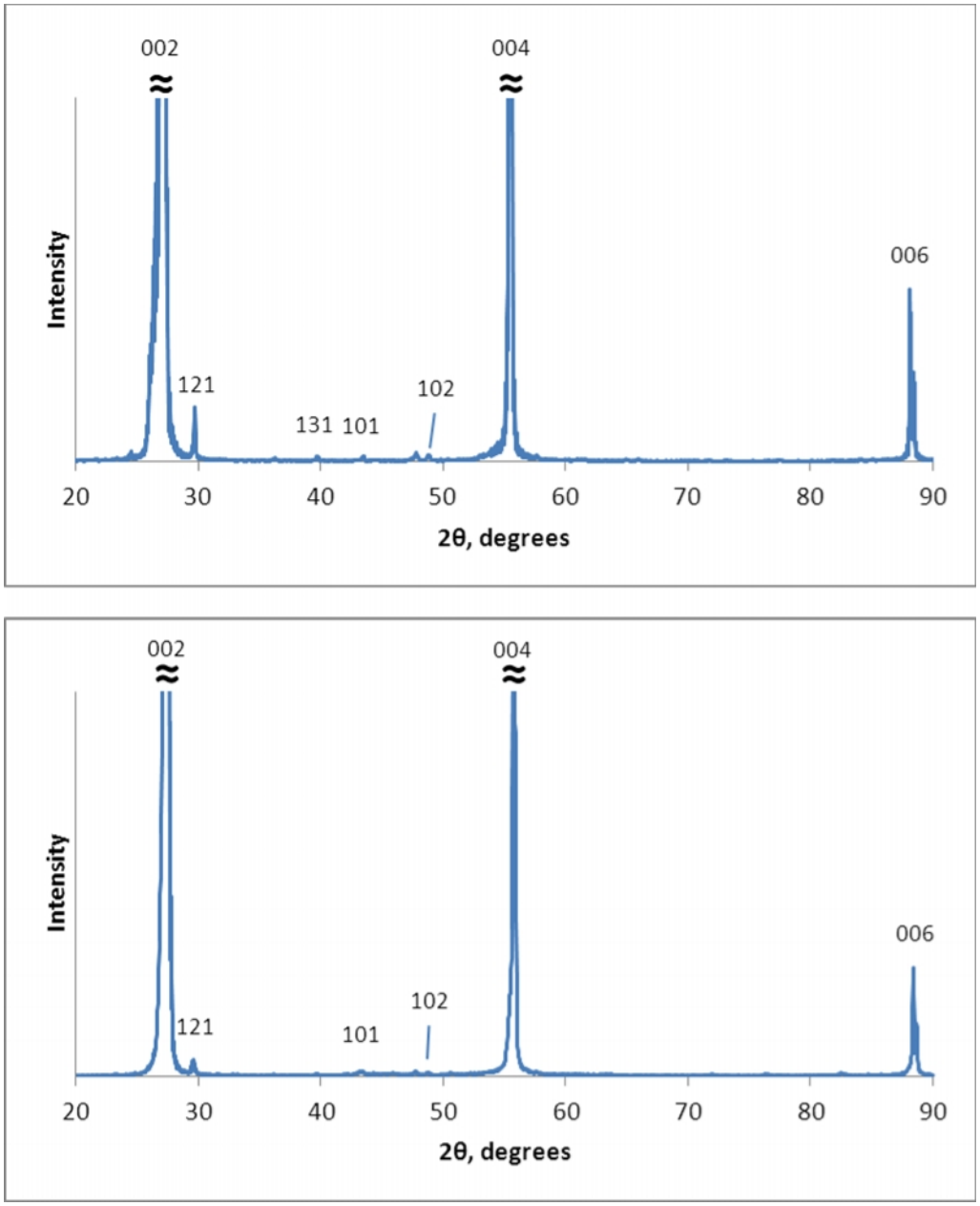

Figure 3-7 XRD spectra of hBN crystals precipitated from soak temperatures of 1550°C (top) and 1700°C (bottom). The FWHM for the 002 peak at 1550°C is 0.60° and at 1700°C 0.31°. Known crystallographic planes of hBN are labeled above their corresponding peaks in the spectra.

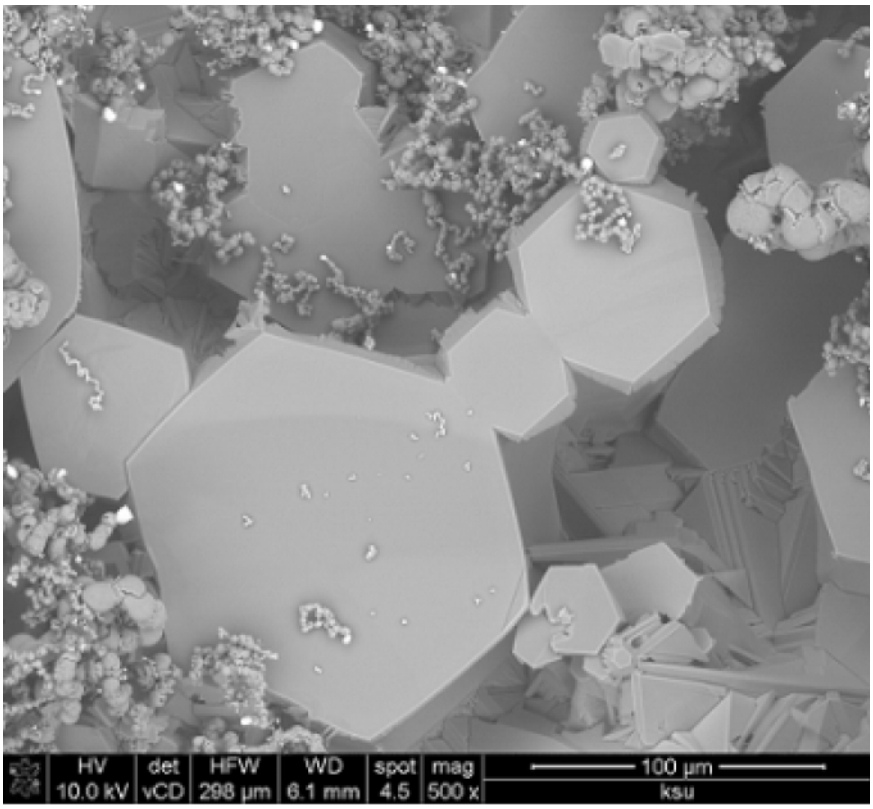

Figure 3-8 SEM image of hBN crystals crystallized with soak temperature of 1475°C. The spots on and around the crystals are residual BN powder. EDS confirms the hBN crystals have a 1:1 boron/nitrogen stoichiometry.

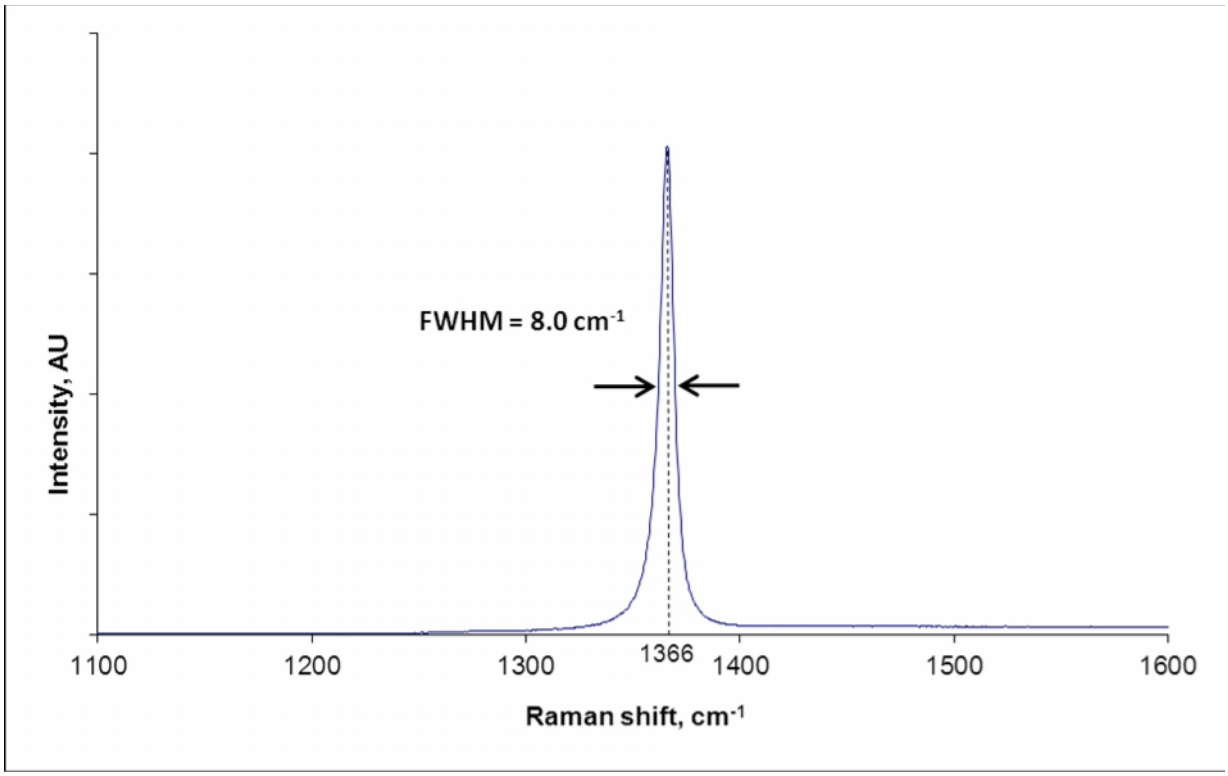

Figure 3-9 Raman spectrum of hBN crystals synthesized at 1450°C. Peak positioned at 1366 cm^{-1} with a full width at half maximum (FWHM) of 8.0 cm^{-1}.

The original BN powder was also characterized to better understand its impurity concentrations. An elemental analysis by LECO Corporation showed the original, untreated boron nitride powder had an average carbon and oxygen concentration of 0.0076% and 0.1035%, respectively. To achieve higher purities, some BN powder was baked at high temperatures (>1900°C) for two hours under nitrogen to drive away carbon and oxygen. Subsequent elemental analysis on these samples showed a 75% reduction in carbon impurities and 42% reduction in oxygen impurities when the high temperature bake was performed in the tungsten furnace. These samples did not change color, but BN powder similarly baked in the graphite furnace turned yellow, alluding to carbon contamination.(*66*) This sample was too small in quantity to perform an accurate elemental analysis, but photoluminescence provided some insight as described below. Therefore, baking the BN powder at 1900°C in the tungsten furnace was effective in reducing impurities in the Ni-Cr-BN system.

Photoluminescence (PL) studies were taken from boron nitride powder to assess its impurities qualitatively. In Figure 3-10, the PL spectrum for untreated BN powder displays a strong, broad peak around 5.4 to 5.8 eV and smaller peaks in the 3.5 to 4.1 eV range. Recent PL

studies on hBN have been performed by others(*6*, *7*, *55–57*) and point to a direct band gap of ~6.0 eV for single crystal hBN. Therefore, the peaks at ~5.5 eV are probably defect-induced and those at lower energies brought about by impurities. PL spectra for BN powder baked at high temperatures to drive away impurities are also shown in Figure 3-10. Notice that the lower energy peaks became stronger when baked in the carbon environment of the graphite furnace. As mentioned before, this yellow colored BN powder likely became contaminated with carbon, thus the lower energy peaks can be attributed to carbon impurities. When the BN powder was baked in a cleaner environment (ie. the tungsten furnace), the lower energy peaks disappear. As for the multiple strong peaks at higher energies, they are likely due to structural defects.(*6*, *7*, *55*) The highest energy peak at 5.73 eV suggests that this is the band gap of BN powder.

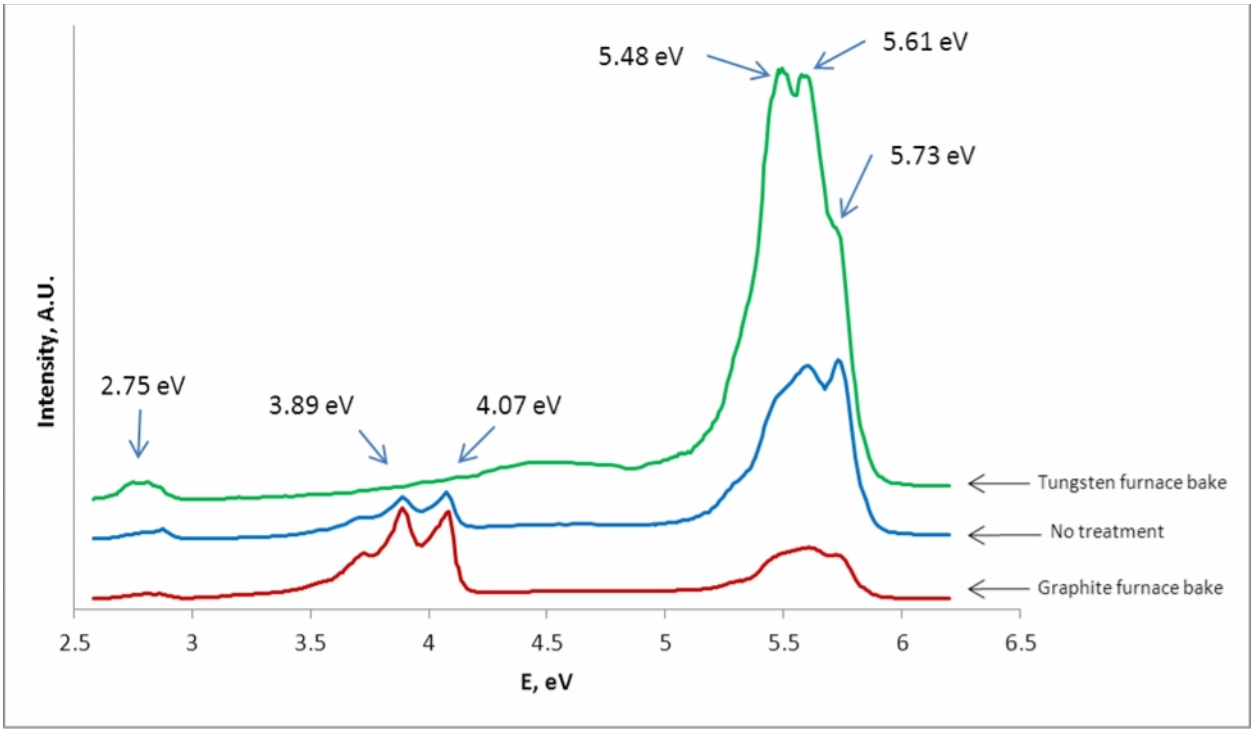

Figure 3-10 Photoluminescence spectra (T = 300K) of boron nitride powder before ("no treatment") and after high temperature bake ("graphite furnace bake" and "tungsten furnace bake") to drive off carbon and oxygen impurities.

Crystals of hBN were also studied by photoluminescence, and the results are shown in Figure 3-11 and Figure 3-12. Not surprisingly, hBN crystals precipitated from carbon-contaminated BN powder exhibited PL peaks characteristic of carbon impurities. However, PL of hBN crystals precipitated from untreated BN powder displayed no characteristic impurity

peaks even though that of the BN powder did (see Figure 3-10). Figure 3-11 suggests that when little carbon is present, it may not segregate to the metal solution. Only in a high-carbon concentration environment (i.e. the graphite furnace) were peaks between 3.5 and 4.0 eV present in the crystals.

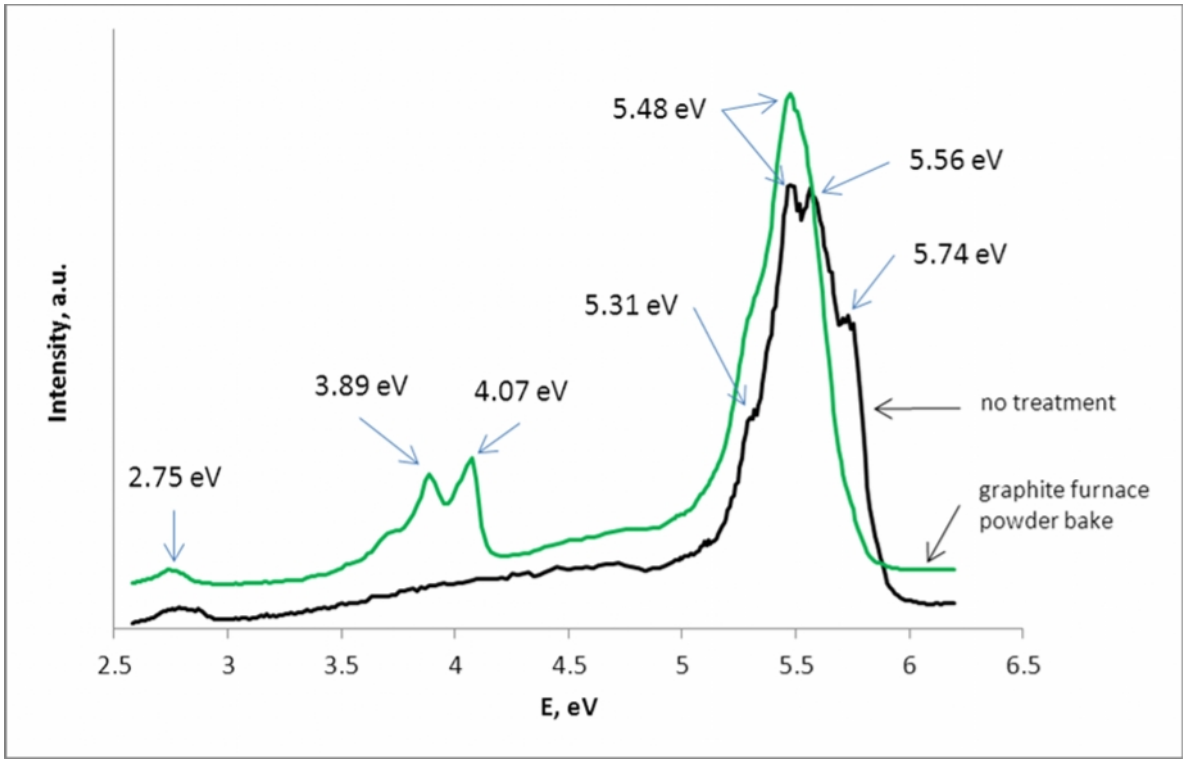

Figure 3-11 Photoluminescence spectra (T = 300K) of hBN crystals precipitated from BN powder that was baked in graphite furnace at 1950°C for 2 hours ("graphite furnace powder bake") and BN powder that was not baked ("no treatment").

The PL spectra in Figure 3-12 are from two samples: an hBN crystal grown at 1500°C for 24 hours that was subsequently annealed at 2000°C for two hours, and a crystal grown at 1700°C for six hours. Both crystals were grown from medium-purity nickel and chromium, so peaks in the 3.90 to 4.1 eV range are likely due to impurities. The peaks at 4.45, 5.33, 5.46 and 5.62 eV are common in PL spectra of hBN grown from high-purity reactants, and thus are probably due to structural defects in the crystal. The annealed crystal in Figure 3-12 has a stronger PL peak in the 5.5 to 5.62 eV range than the other crystal, suggesting that annealing improved crystal quality to some extent, but did not repair all defect sites.

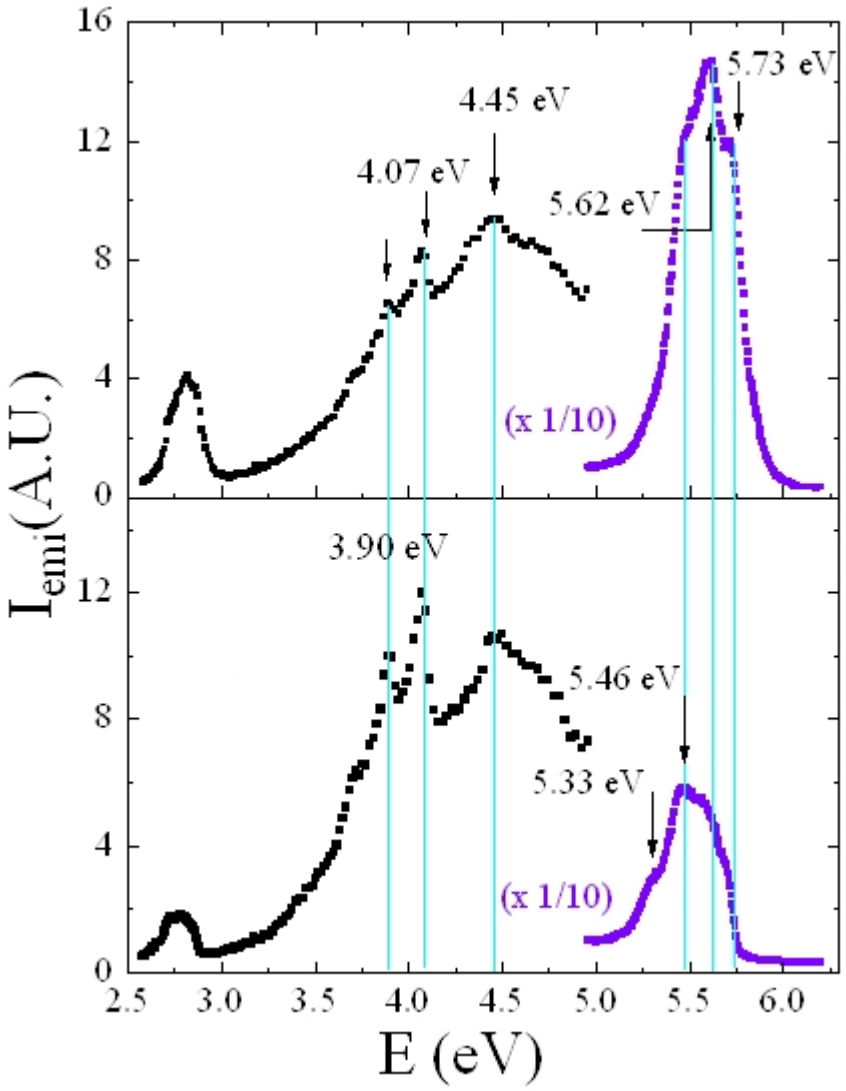

Figure 3-12 Photoluminescence spectra (T = 300K) of hBN crystal annealed in tungsten furnace at 2000°C for 2 hours (top) and hBN crystal precipitated from BN powder dissolved in Ni-Cr at 1700°C for 6 hours in graphite furnace (bottom).

Direct hBN synthesis from boron powder and nitrogen compound in metal solvent

After successfully growing >5 millimeter-wide hBN crystals by the precipitation method with BN powder precursor, interest shifted to directly synthesizing hBN from elemental boron and nitrogen. Results of the hBN synthesis experiments with boron powder dissolved in pure nickel, nickel-chromium, and pure copper solvents are presented next along with some key observations and characterizations of samples.

Growth conditions and observations

In contrast to hBN crystal growth from BN powder, synthesizing hBN from an elemental boron source and a nitrogen source (ammonia or nitrogen) has not previously been reported. This method is appealing because it enables crystal growth of isotopically enriched hBN single crystals with boron-10, the isotope of interest for neutron detection. Following the success of the Ni-Cr solvent with BN powder, it was natural to extend its use to a direct synthesis method. For comparison, pure nickel and pure copper solvents were also tested.

The results of all direct synthesis experiments where soak temperatures, times, cooling rates and nitrogen source were adjusted are summarized in Table 3-1. One would expect the conditions that produced the largest crystals in the Ni-Cr-BN system would also produce large crystals in the Ni-Cr-B system, and this appears to be the case: higher temperatures produce larger crystals. A nickel-chromium-boron eutectic mixture of 65.6 at% nickel, 16.1 at% chromium and 18.3 at% boron under nitrogen atmosphere produced the largest hBN crystal, with a width of 900 μm and a thickness close to 150 μm. The photos in Figure 3-13a-c display a soak temperature progression of hBN synthesis, with the largest crystals synthesized from high-purity nickel and chromium highlighted in Figure 3-13c. Nucleation appeared prominent at 1400°C (Figure 3-13b) as many small crystallites formed but were not able to expand due to crowding. The soak at 1525°C improved crystal size, and higher temperatures would likely grow even larger crystals. However, due to the temperature limitation of the alumina tube in the CM furnace, temperatures higher than 1525°C were not possible.

Ammonia was tested as a nitrogen precursor to increase nitrogen concentration in the metal solvent due to its low dissociation temperature compared to N_2. No advantages of ammonia were evident from the experiments. The high temperatures likely caused ammonia to immediately dissociate and recombine as N_2 and H_2, thereby diluting the nitrogen concentration in the system. In light of this and ammonia's safety hazards, it was replaced with N_2.

Pure nickel and copper solvents were also tested because of their attractive reactivity with acids that make isolating the hBN crystals from these metals easier than from Ni-Cr. However, these did not yield hBN due to their low nitrogen solubilities.(*39*, *40*) The copper system did yield small dark crystals which are presumably boron.

Table 3-1 Conditions and results from direct hBN synthesis experiments

Solvent	*Nitrogen Source*	*Soak Temperature (°C)*	*Soak time (hr)*	*Cooling rate (°C/hr)*	*Crystal width*
Ni-Cr	NH_3	1100-1200	12	8	none
		1300	12	8	<20 μm
		1400	12	4	<500 μm
	N_2	1525	6	4	900 μm
Ni	NH_3	1100-1300	12	8	none
		1400	12	8	<20 μm
	N_2	1150-1400	12	4-8	none
Cu	NH_3	1400	12	8	none
	N_2	1500	12	6	No hBN

Note: The boron source for all experiments was boron powder

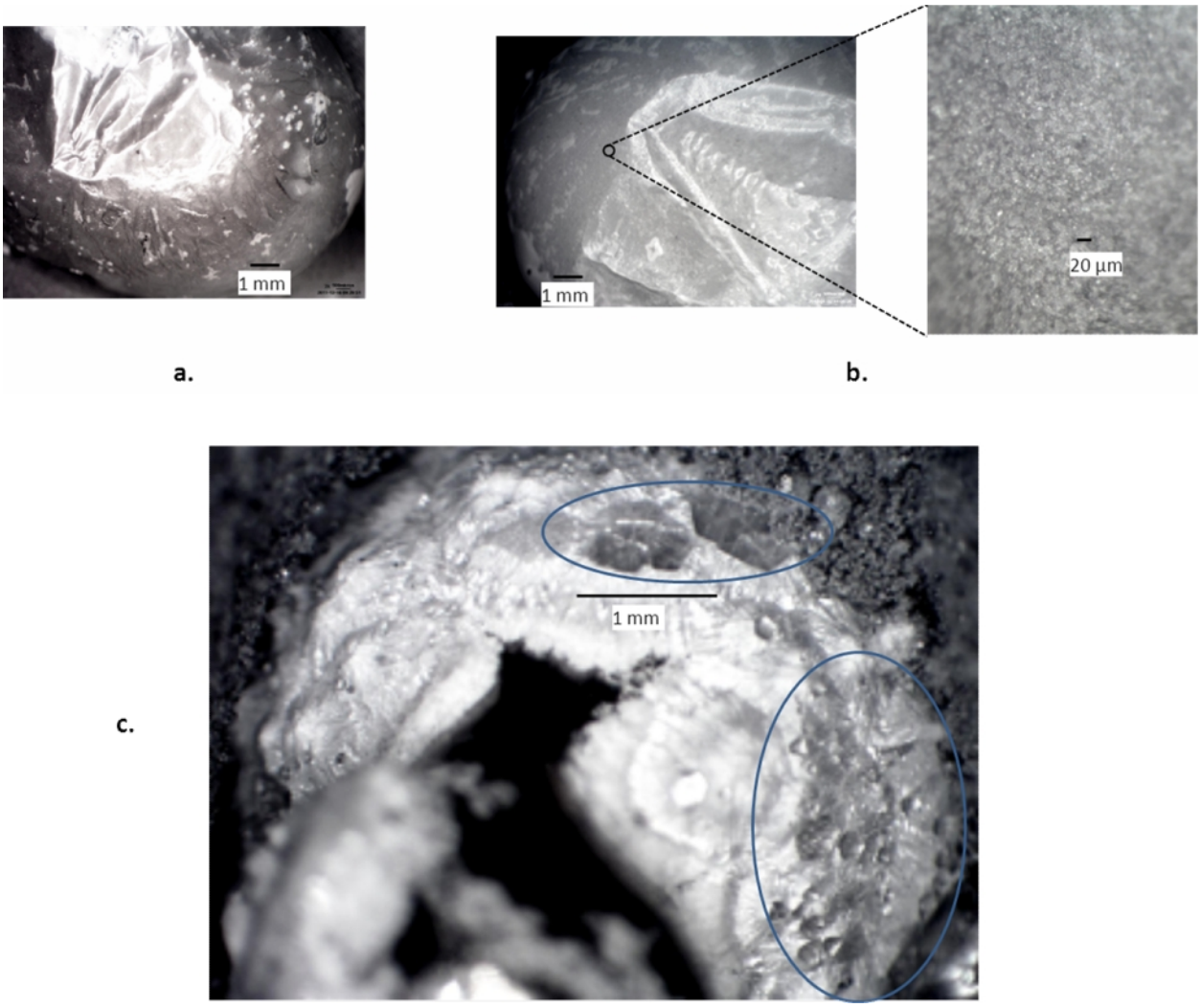

Figure 3-13 Photos of direct hBN synthesis from boron powder in nickel-chromium solvent a.) 1300°C under NH_3 b.) 1400°C under NH_3 and c.) 1525°C under N_2. The circled areas are the largest hBN crystals synthesized by this method.

Characterizations of hBN

The XRD pattern from hBN directly synthesized from boron powder in nickel-chromium solvent is shown in Figure 3-14. The two spectra represent hBN synthesized at soak temperatures of 1200°C (bottom) and 1400°C (top) under ammonia. These crystals formed a thin crust over the nickel-chromium solvent from which they could not be easily separated. Thus, many of the peaks in the spectra can be attributed to the metal boride phases. Clearly, higher soak temperatures increase the likelihood of hBN forming as indicated by the height of the (002) peak at 26.8° and the (004) peak at 55.1°.

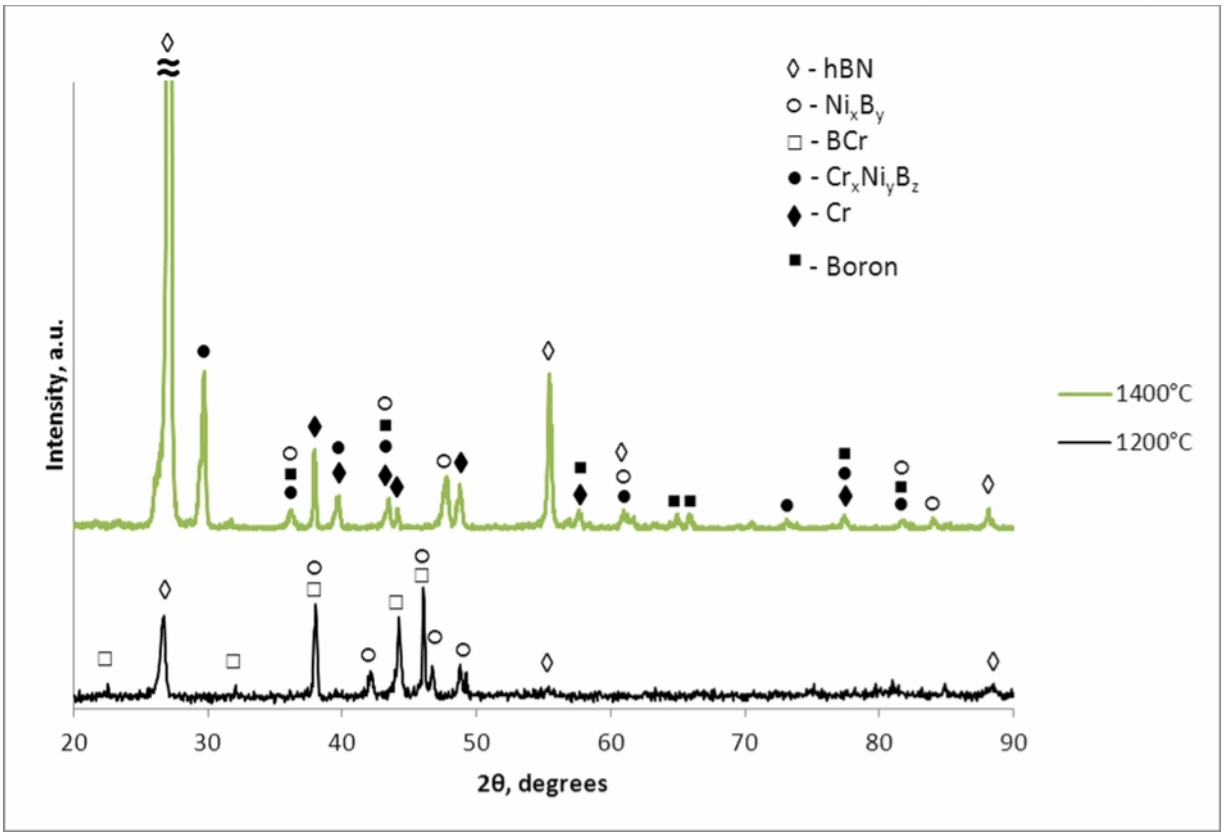

Figure 3-14 XRD spectra of hBN directly synthesized from boron powder in Ni-Cr and ammonia at 1200°C (bottom) and 1400°C (top). hBN samples were not removed from the solidified Ni-Cr solvent, thus many of the peaks in the spectra can be assigned to solvent phases.

The small width and thickness of the hBN crystals suggests the solvent was starved for nitrogen. Since ammonia was introduced in these experiments after the system reached its soak temperature, subsequent experiments were performed under a nitrogen atmosphere for the entire duration of the experiment. The large crystals depicted in Figure 3-13c were grown with nitrogen continuously flowing through the system throughout the ramp and soak periods of the experiment, thus proving that nitrogen dissolution in the solvent is key to large crystals. An XRD spectrum of these large hBN crystals is shown in Figure 3-15. These crystals were isolated from the metal solvent, and because of the small sample size, the peak intensities in Figure 3-15 are diminished compared to the XRD spectra in Figure 3-7. Nonetheless, the (002) peak is prominent in the spectrum and is a good indicator that the crystals are in fact high-quality hBN.

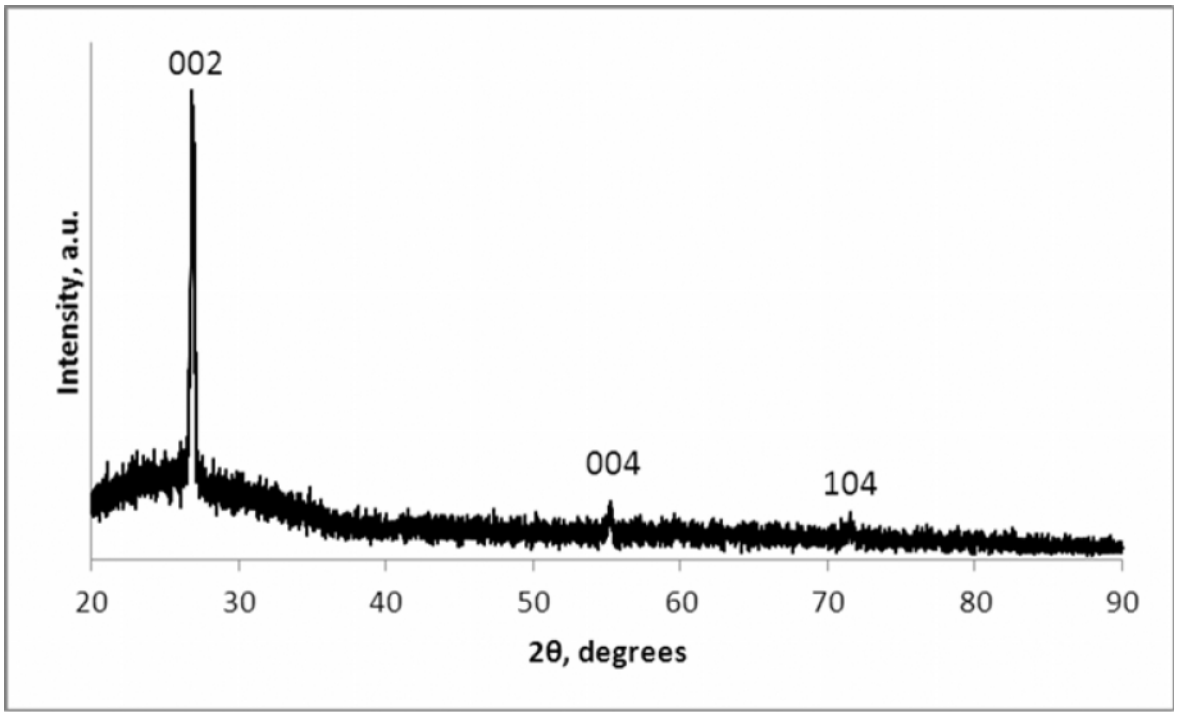

Figure 3-15 XRD spectrum of hBN synthesized from boron powder and nitrogen in Ni-Cr at 1525°C. The broad peak from 20-40° is due to the glass sample holder. Known crystallographic planes of hBN are labeled above their corresponding peaks in the spectrum.

A photoluminescence spectrum of the hBN crystals in Figure 3-13c is shown in Figure 3-16 as well as a spectrum of hBN grown from BN powder for comparison. The spectrum was dominated by a peak at 5.73 eV, the highest of any hBN crystals produced in this study and close to 5.77 eV (215 nm) reported by others(*6*, *41*, *43*). This could indicate less strain and better long range order in the directly synthesized crystal. Both hBN crystals were precipitated from high-purity nickel and chromium metal, so the broad peak at 4.42 eV could stem from structural defects.

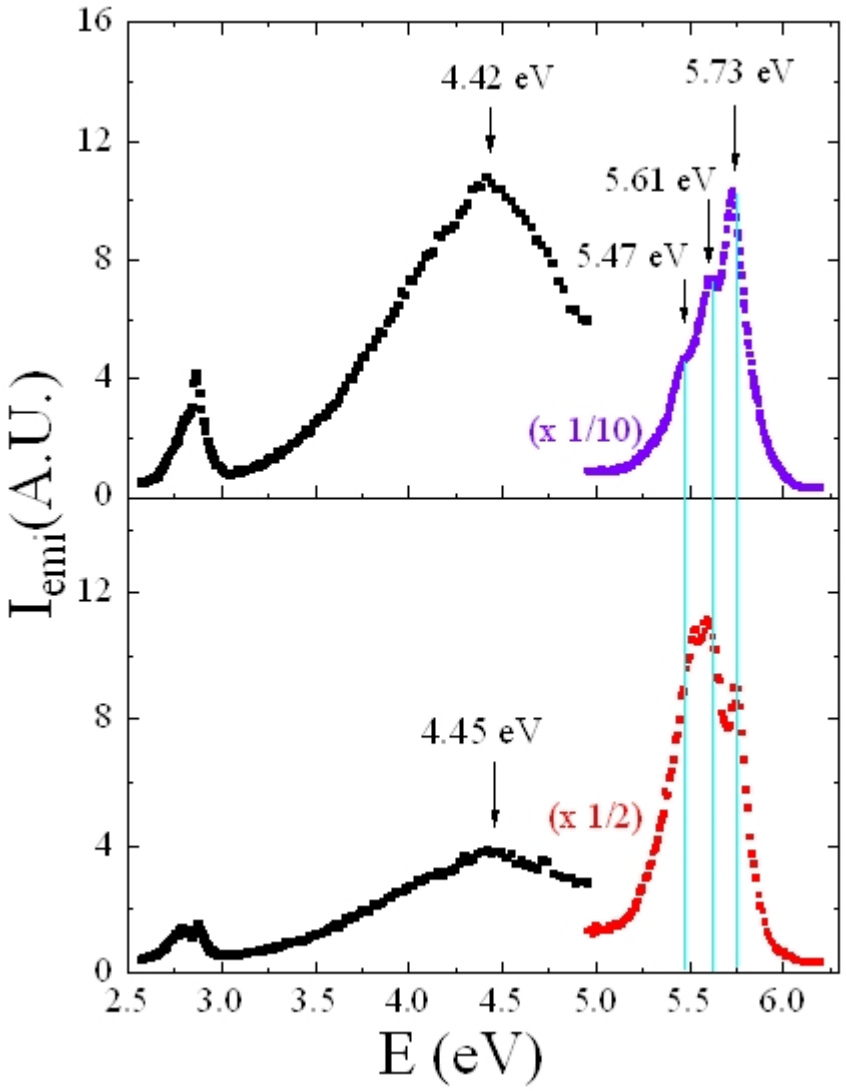

Figure 3-16 Photoluminescence spectra (T = 300K) of hBN synthesized from boron powder and nitrogen at 1525°C (top) and hBN precipitated from BN powder dissolved in Ni-Cr at 1525°C (bottom).

Analysis of Structural Defects

All crystalline solids have imperfections that range from point defects (atomic substitutions or vacancies) to volume defects (voids or precipitates). Electrical devices require highly ordered material with low defects, so defect-selective etching was employed and TEM images taken to qualitatively assess the crystal quality of some hBN crystals. Only a few etching studies on hexagonal and cubic phases of BN have been reported(*58*, *59*), along with TEM

studies of epitaxial or monolayers of hBN(*67*, *68*). No comprehensive studies on defect selective etching or TEM imaging of bulk single crystal hBN have been reported in the literature.

Defect-selective etching of hBN

Several etchants were tested in the present study. Sodium nitrate at temperatures between 300°C and 400°C did not etch hBN crystals. Molten KOH between 400°C and 500°C etched hBN easily, but too much so. A eutectic of potassium hydroxide/sodium hydroxide proved to be most effective at temperatures around 450°C. All etch pits formed on the (0001) crystal plane.

A molten eutectic mixture of potassium hydroxide and sodium hydroxide is an effective etchant for many crystalline materials(*58*, *61–64*), but the proper amount of etching is strongly dependent on the temperature of the etchant and the amount of time hBN is subject to the molten alkali(*69*). Etching temperature was investigated first, holding etching time constant. Figure 3-17 and Figure 3-18 are SEM images of hBN crystals etched at 400°C, 450°C and 500°C for one minute. Etch pits that overlap as those in the bottom image of Figure 3-17 do are not desirable because this complicates the calculation of the etch pit density (EPD). Therefore, 500°C is too high a temperature when etching for one minute. Looking at the top image in the same figure, no etch pits were discernible at 400°C, suggesting this temperature is too low to be effective. The etched hBN in Figure 3-18 at 450°C is better for calculating EPD, although perhaps not optimal since some etch pits overlap. Nonetheless, an average EPD of ~5 x 10^6 cm^{-2} was calculated for these hBN crystals, which is comparable to typical semiconductor-grade GaAs (~10^5 cm^{-2}).(*70*) Figure 3-19 illustrates the effect of time on the etching pattern. For a short time of 0.5 minute, the etch pits are separate and distinct, but their complete morphology has not developed (hexagonal sides and pointed bottom). However, etch pits formed after etching for 1.5 minutes overlap, and the etchant aggressively attacks grain boundaries and other planar defects. From these observations, the proper etching conditions for hBN defect selective etching in eutectic KOH/NaOH appear to be 430-450°C for 0.5-1 minute.

All etch pits from this etching study were hexagonal, as we would expect for a hexagonal crystal system. Figure 3-20 provides a magnified view of some hexagonal etch pits. Two distinct types of hexagonal pits formed: deep, point-bottom pits (labeled ***A***) and shallow, flat-bottom pits (labeled ***B***). While not easy to ascertain, the pointed-bottom pits appear to be slightly asymmetric, suggesting a mixed-type (screw and edge) dislocation.(*69*) The defect

associated with the flat-bottom pits are unknown; possibilities are discussed below. The aforementioned etch pit characteristics of hBN are also seen in chemically etched single-crystal graphite(*60*, *71*) and SiC(*63*), so in the absence of major etching studies on hBN, comparisons with these materials similar in structure to hBN are appropriate.

Weyher et al.(*63*) reported two types of hexagonal etch pits and an oblong shell-like pit in Si-C after etching in KOH/NaOH + MgO. They attributed the deep hexagonal pits to screw dislocations, the smaller hexagonal pits to edge dislocations, and the shallow, oblong shell-like pits to basal plane dislocations. Only the two types of hexagonal pits Weyher et al. described are visible in Figure 3-20. Etch lines are also seen in Figure 3-20 (labeled ***C***), which in SiC indicated the presence of stacking faults.(*63*) These lamellae in SiC are typically bordered by the oblong etch pits of basal plane dislocations, but this is not observed in Figure 3-20. In fact, the lines appear to terminate at the shallow hexagonal pits more often than not. Also noteworthy is the etch lines in SiC are very straight, whereas those in Figure 3-20 are not. By these observations, the flat-bottom pits are probably not associated with basal plane dislocations.

The feature denoted by ***D*** in Figure 3-20 is interesting because the deep and shallow hexagonal etch pits appear to overlap. This phenomenon is seen in chemically etched single crystal graphite as well and attributed to a jog in the dislocation, where the dislocation abruptly moves in a direction perpendicular to the c-axis before continuing along its usual path parallel to the c-axis(*71*). Therefore, the flat-bottom pits could be due to shallow screw dislocations that have completely etched under these conditions.

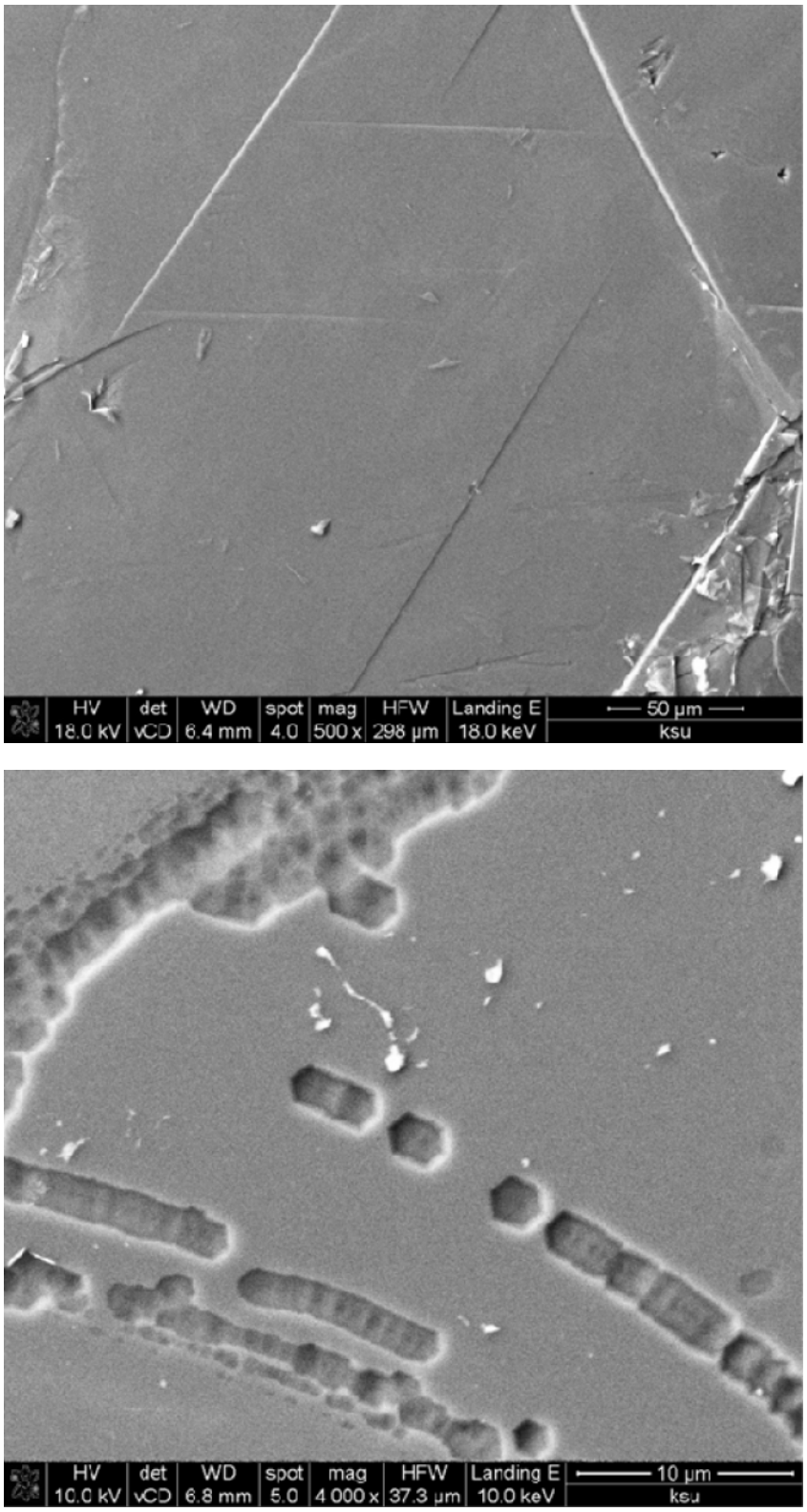

Figure 3-17 SEM images of hBN etched in KOH/NaOH at 400°C (top) and 500°C (bottom) for one minute.

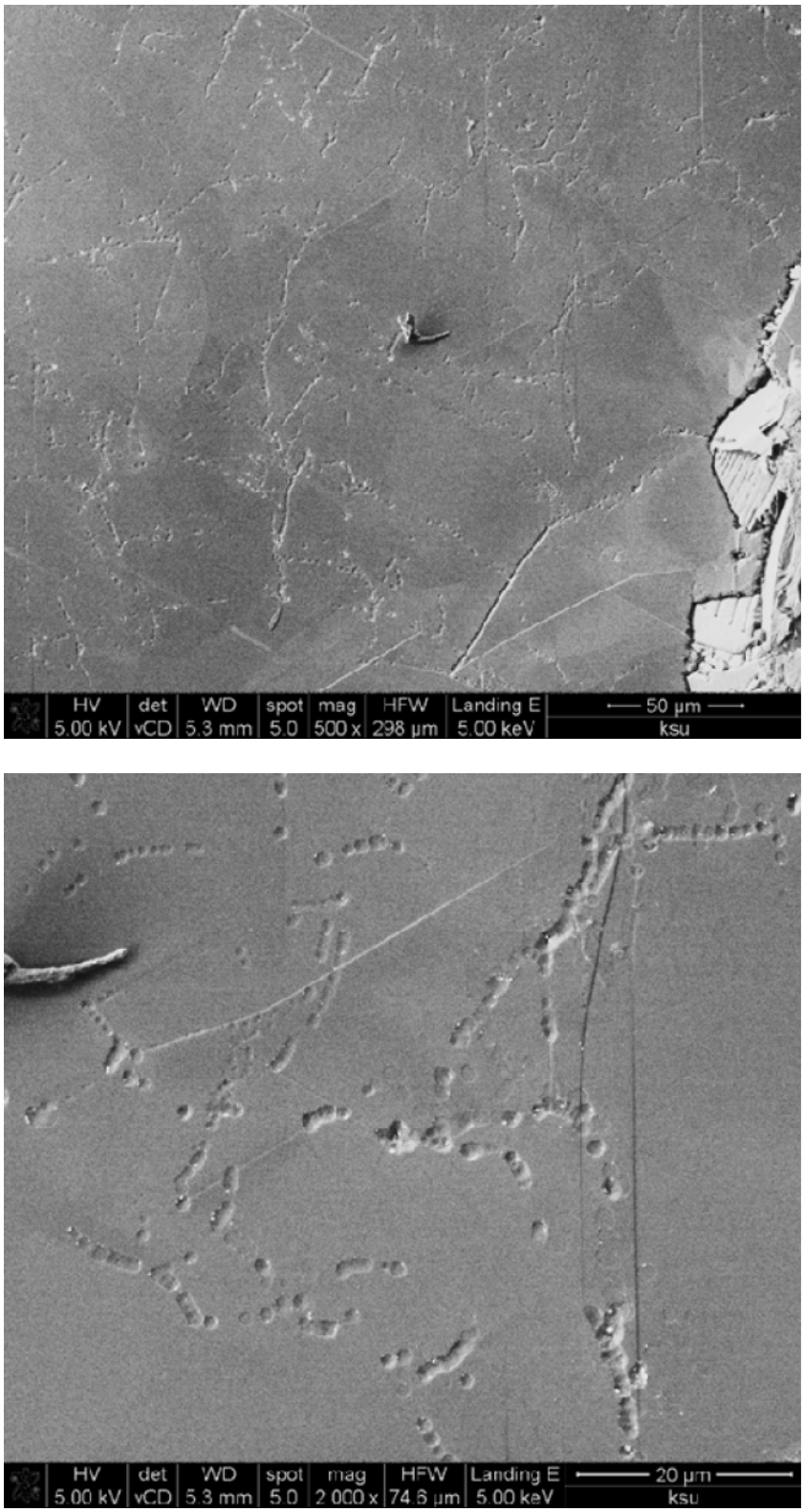

Figure 3-18 SEM image of hBN etched at 450°C for one minute in KOH/NaOH under low magnification (top) and high magnification (bottom).

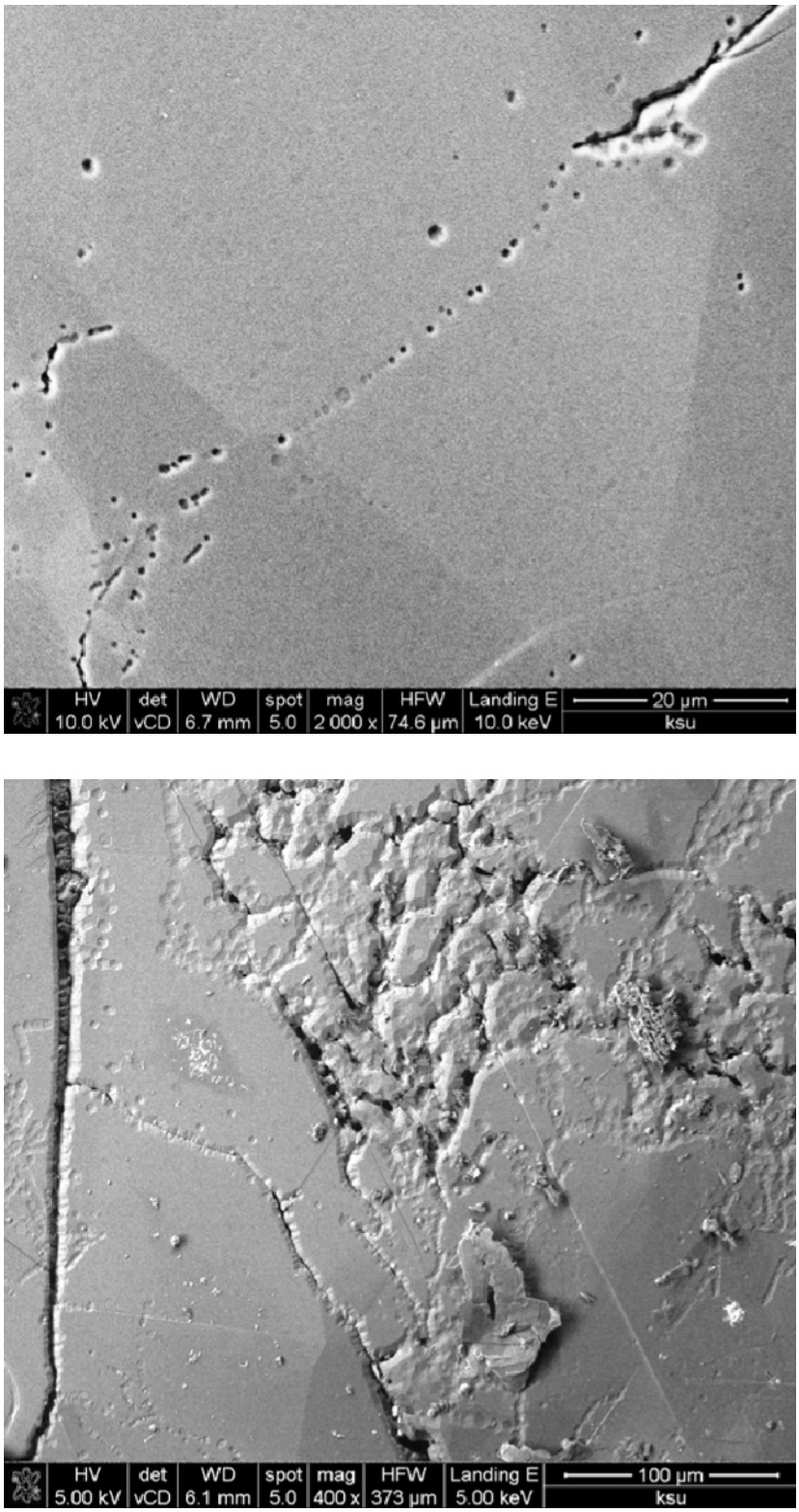

Figure 3-19 SEM image of hBN etched in KOH/NaOH at 430°C for 0.5 minutes (top) and 1.5 minutes (bottom).

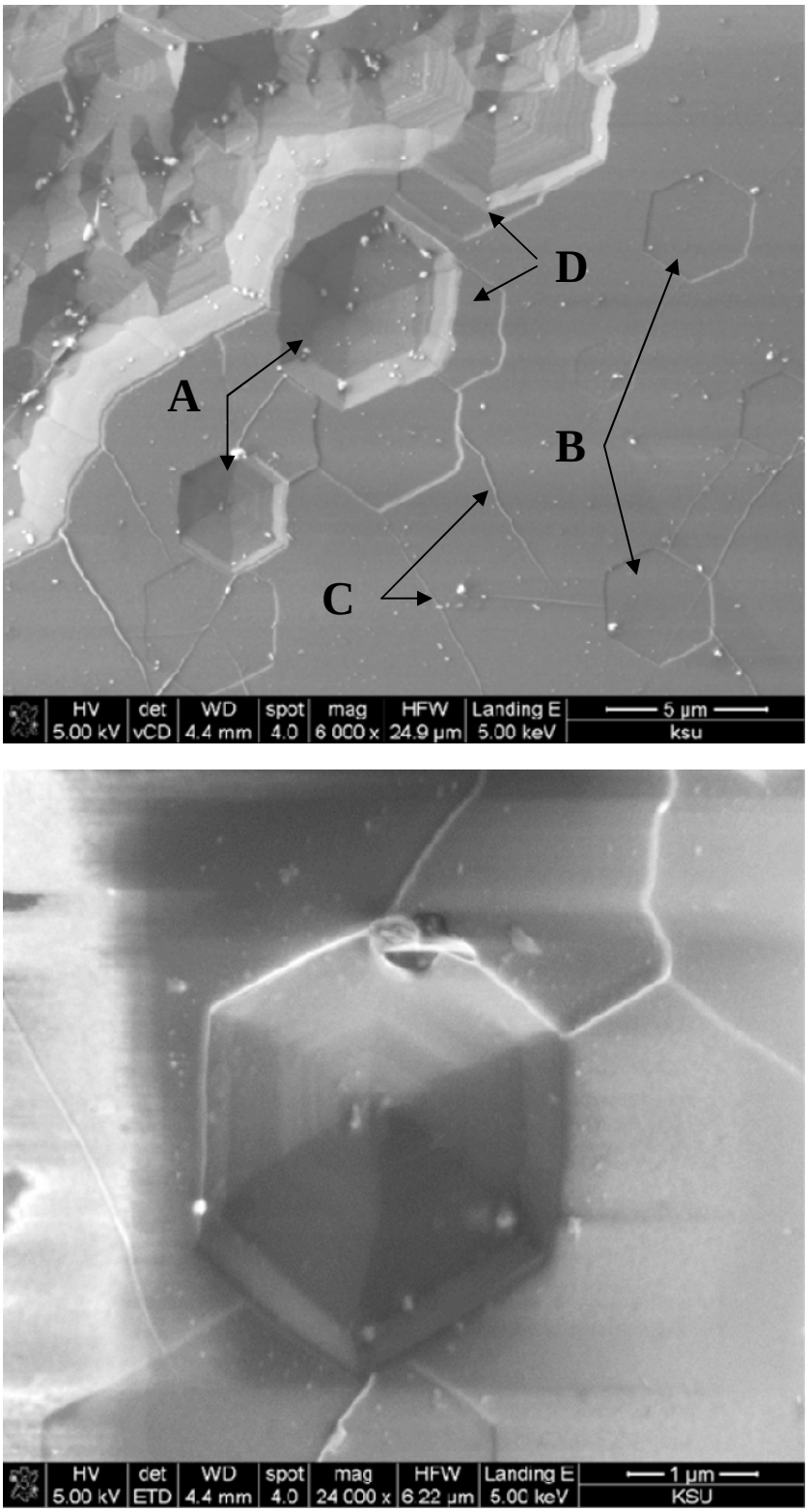

Figure 3-20 Low magnification (top) and high magnification (bottom) SEM images of etch pits in hBN after KOH/NaOH etch at 430°C for 1.5 minutes. The features labeled *A*-*D* are discussed in the text.

TEM imaging of hBN

The TEM images in Figure 3-21 and Figure 3-22 reveal some interesting features in the hBN crystals. In Figure 3-21*i*., the basal plane layers of hBN (denoted ***A***) are clearly seen. A band of misoriented hBN also appears (denoted ***B***) from unknown origins. The contrast in Figure 3-21*ii.* shows a junction of many basal plane orientations. Figure 3-23 illustrates one of these possible misorientations with respect to the preferred orientation of hBN, with others being slight variations. The features labeled ***C*** in Figure 3-21 are presumed to be dislocation loops as they are nearly identical to those seen in graphite.(*72*) In Figure 3-21*iv.*, a TEM image of an hBN crystal synthesized at high soak temperatures is shown. On qualitative grounds, the number of defects (specifically, dislocation loops and basal plane dislocations) is lower for this sample than for samples synthesized at lower temperatures. But the presence of Moire fringes suggests that the higher temperature did not correct the tendency of basal planes to rotate with respect to each other.

Figure 3-22*i.* and *ii.* display some interesting patterns; the continuous lines across the image (denoted ***A***) are Moire fringes from slight rotational differences among hBN layers (confirmed by multiple diffraction spots in the SAED patterns in *iii.* and *iv.*), and the darker lines (denoted ***B***) are basal plane dislocations. The basal plane dislocations are suspected to be the lines of intersection between two different basal orientations, such as the two orientations depicted in Figure 3-23a and Figure 3-23c. Studies in structurally-similar graphite show that basal plane dislocations can be brought about by stacking faults.(*73*) The multiple diffraction spots in Figure 3-22*iv*. suggest that at least some of the basal planes of hBN orient their layer-to-layer atoms slightly off-center as opposed to stacking the atoms center-to-center (Figure 3-23b).

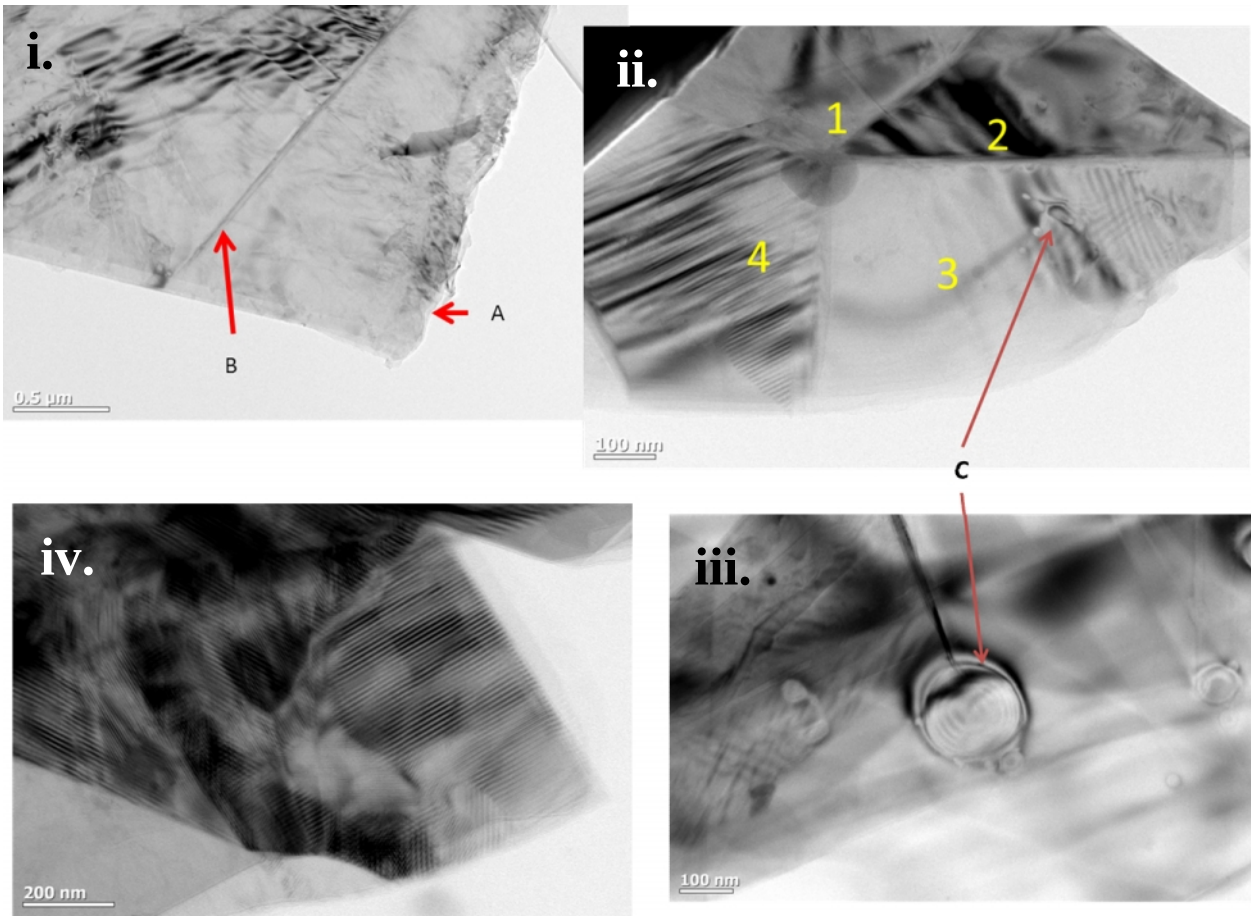

Figure 3-21 TEM images of hBN crystals. i.) Flake of hBN synthesized at 1500°C with basal planes visible (A) and a band of misoriented material (B); ii.) hBN synthesized at 1500°C with four distinct regions of basal plane orientations (1-4) and dislocation loops (C); iii.) Close-up of vacancy loop feature in ii.); iv.) hBN synthesized at 1700°C.

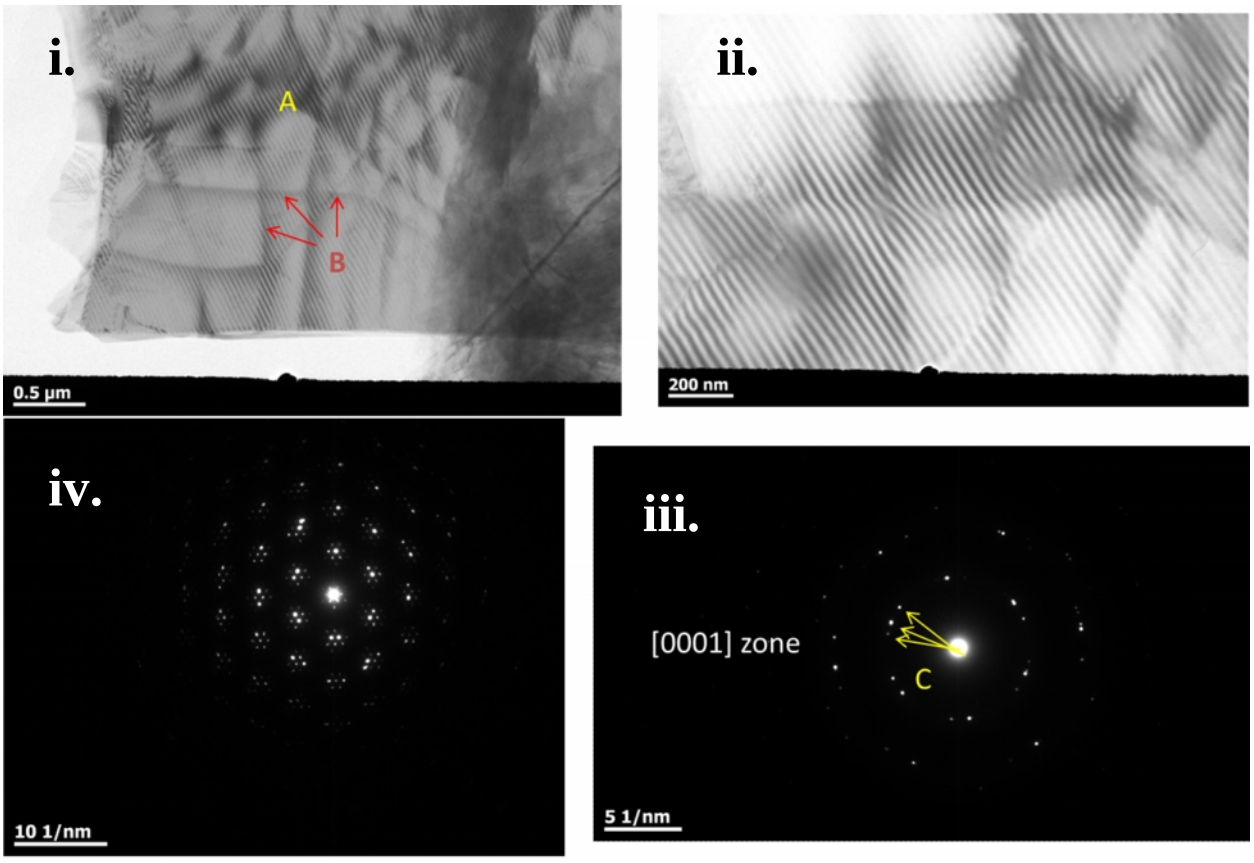

Figure 3-22 i.) TEM image of hBN synthesized at 1475°C with Moire fringes (A) and basal plane dislocations (B) present; ii.) magnified view of i.); iii.) SADP of hBN synthesized at 1475°C with multiple diffraction spots (C); iv.) SADP of hBN synthesized at 1700°C.

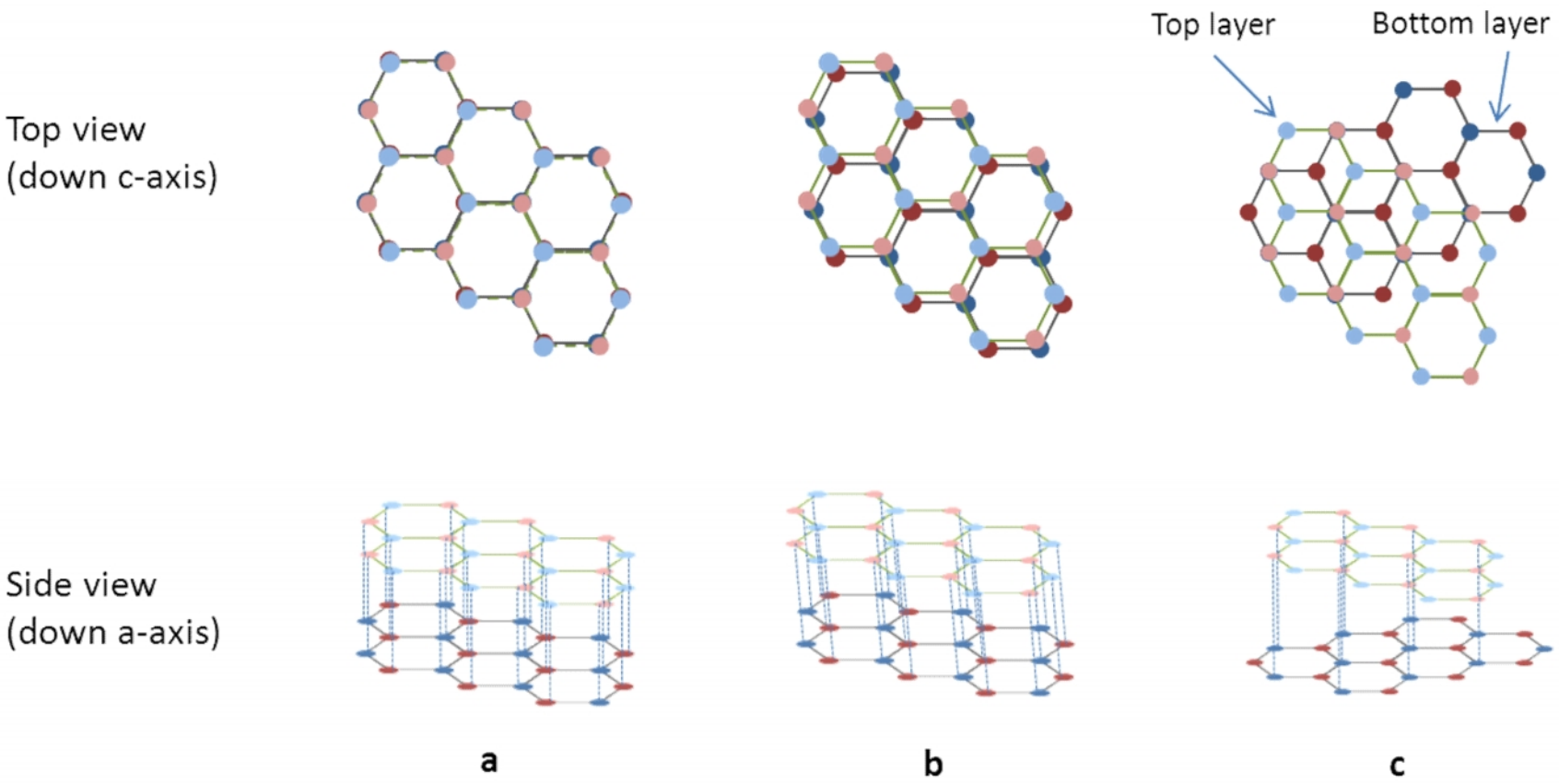

Figure 3-23 Orientations of hBN layers. a.) Thermodynamically-preferred orientation with all boron atom centers atop nitrogen atom centers and vice versa. b.) Orientation in *a.* but with small rotation in one layer so that atom centers are not in line; c.) Orientation similar to *a.* but with 60° rotation and ½-unit translation of bottom layer to maintain stacking order of boron atop nitrogen and vice versa. Not all atoms are paired with atoms in adjacent layers.

Chapter 4 - Conclusions and Recommendations

hBN crystals were grown from metal solvents to explore their potential in neutron detection. The effects of soak temperature, soak time, source materials and their proportions on hBN crystal size and properties were investigated. The largest crystals of hBN from solution growth were five millimeters across and about 30 micrometers thick by precipitation from BN powder dissolved in a nickel-chromium solvent at 1700°C. High temperatures promoted outward growth of the crystal along the a-axis, whereas low temperatures promoted growth along the crystal c-axis. Bulk hBN crystals adopted a triangular habit rather than a hexagonal one when growth temperatures surpassed ~1500°C.

A previously unreported method of synthesizing hBN was proven successful by substituting BN powder with elemental boron and a nitrogen ambient. At temperatures over 1500°C, hBN crystals about one millimeter wide were produced. The success of this growth method opens the door for isotopically-enriched h-^{10}BN important for applications in neutron detection.

XRD and Raman spectroscopy confirmed highly crystalline hBN from solution growth. The 8.0 cm^{-1} FWHM of the Raman peak is the narrowest reported to date. Photoluminescence identified impurities and defects in the hBN samples, but high-purity reactants and post-growth annealing showed promise for synthesizing semiconductor-grade hBN. The highest energy, highest intensity PL peak observed in this study came from hBN synthesized from elemental boron, indicating that this new hBN crystal growth method could be quite promising.

Among sodium nitrate, potassium hydroxide, and a eutectic mixture of KOH/NaOH, the latter was the most effective defect-selective etchant at temperatures of 430-450°C in contact with hBN for about one minute. Two hexagonal etch pit morphologies observed were deep, pointed-bottom pits and shallow, flat-bottom pits. More experimentation is necessary to correlate etch pits with their associated defects, such as etching cleaved crystals and identifying the specific defects associated with specific types of etch pits by, for example, TEM. Basal plane twists and dislocations were evident in TEM images and SAED patterns of hBN crystals, but whether this affects hBN's usefulness as an electronic device remains to be seen.

To fully realize the potential hBN has as a neutron detector, a method by which metal contact pads can be placed on hBN is necessary to evaluate its electrical properties. Focused ion

beam metal wire bonding may be the most promising technique for small crystals. Although hBN with natural isotopic abundance is believed to be adequate for neutron detection, $h^{10}BN$ could be grown to increase neutron detection efficiency. While five millimeter wide hBN crystals are the largest reported so far, even larger crystals (>1 cm^2) would benefit device fabrication and neutron detection efficiency in low emission settings.

References

(1) Balmain, W. H. Bemerkungen über die Bildung von Verbindungen des Bors und Siliciums mit Stickstoff und gewissen Metallen. *J Prakt Chem* **1842**, *27*, 422-430.

(2) Haubner, R.; Wilhelm, M.; Weissenbacher, R.; Lux, B. Boron Nitrides - Properties, Synthesis and Applications. *High Performance Non-oxide Ceramics II* **2002**, *102*, 1–45.

(3) Lipp, A.; Schwetz, K. A.; Hunold, K. Hexagonal boron nitride: Fabrication, properties and applications. *Journal of the European Ceramic Society* **1989**, *5*, 3-9.

(4) Bundy, F. P.; Wentorf, R. H. Direct Transformation of Hexagonal Boron Nitride to Denser Forms. *The Journal of Chemical Physics* **1963**, *38*, 1144.

(5) Corrigan, F. R.; Bundy, F. P. Direct transitions among the allotropic forms of boron nitride at high pressures and temperatures. *The Journal of Chemical Physics* **1975**, *63*, 3812-3820.

(6) Watanabe, K.; Taniguchi, T.; Kanda, H. Direct-bandgap properties and evidence for ultraviolet lasing of hexagonal boron nitride single crystal. *Nature Materials* **2004**, *3*, 404-9.

(7) Museur, L.; Brasse, G.; Pierret, A.; Maine, S.; Attal-Tretout, B.; Ducastelle, F.; Loiseau, A.; Barjon, J.; Watanabe, K.; Taniguchi, T.; Kanaev, A. Exciton and interband optical transitions in hBN single crystal. *ArXiv e-prints* **2011**, 1-12.

(8) Gannett, W.; Regan, W.; Watanabe, K.; Taniguchi, T.; Crommie, M. F.; Zettl, A. Boron nitride substrates for high mobility chemical vapor deposited graphene. *Applied Physics Letters* **2011**, *98*, 1-3.

(9) Edgar, J. H. Crystal structure, mechanical properties, and thermal properties of BN. In *Properties of Group III Nitrides*; Edgar, J. H., Ed.; EMIS Datareview Series No. 11 INSPEC, 1994.

(10) Lopatin, V. V. Electrical transport properties of BN. In *Properties of Group III Nitrides*; Edgar, J. H., Ed.; EMIS Datareview Series No. 11 INSPEC, 1994.

(11) Jaszczak, J. Graphite Properties. http://www.phy.mtu.edu/~jaszczak/graphprop.html (accessed March 14, 2012).

(12) Spriggs, G. E. 13 . 5 Properties of diamond and cubic boron nitride. In *Landolt-Börnstein - Group VIII Advanced Materials and Technologies*; Beiss, P.; Ruthardt, R.; Warlimont, H., Eds.; Springer Materials; Vol. A.

(13) Yamaguchi, E. Thin film boron nitride for semiconductor application. *Materials Science Forum* **1991**, *54-55*, 329-352.

(14) Wang, H.; Taychatanapat, T.; Hsu, A.; Watanabe, K.; Taniguchi, T.; Jarillo-Herrero, P.; Palacios, T. BN/Graphene/BN Transistors for RF Applications. *Electron Device Letters, IEEE* **2011**, *32*, 1209–1211.

(15) Volpe, G. *Optics and Photonics Focus*. October 2008,.

(16) Watanabe, K.; Taniguchi, T.; Kuroda, T.; Kanda, H. Effects of deformation on band-edge luminescence of hexagonal boron nitride single crystals. *Applied Physics Letters* **2006**, *89*, 1-3.

(17) Watanabe, K.; Taniguchi, T.; Niiyama, T.; Miya, K.; Taniguchi, M. Far-ultraviolet plane-emission handheld device based on hexagonal boron nitride. *Nature Photonics* **2009**, *3*, 591-594.

(18) Crane, T. W.; Baker, M. P. Neutron Detectors. In; pp. 379-406.

(19) Rockwell, M. DNDO closer to Helium-3 alternative for nuclear detection monitors. http://www.gsnmagazine.com/node/24945 (accessed December 8, 2011).

(20) Doty, F. P. *Advanced Digital Detectors for Neutron Imaging*; 2003; pp. 3-16.

(21) Kitaguchi, H.; Miyai, H.; Izumi, S.; Kaihara, A. Silicon semiconductor detectors for various nuclear radiations. *Nuclear Science, IEEE* **1996**, *43*, 1846-1850.

(22) Nikolic, R.; Conway, A.; Reinhardt, C.; Graff, R.; Wang, T.; Deo, N.; Cheung, C. Fabrication of Pillar-structured thermal neutron detectors. *NSS '07 IEEE* **2007**, *2*, 1577-1580.

(23) Robertson, B. W.; Adenwalla, S.; Harken, A.; Welsch, P.; Brand, J. I.; Dowben, P. a.; Claassen, J. P. A class of boron-rich solid-state neutron detectors. *Applied Physics Letters* **2002**, *80*, 3644-3646.

(24) Kumashiro, Y.; Kudo, K.; Matsumoto, K.; Okada, Y.; Koshiro, T. Thermal neutron irradiation experiments on 10BP single-crystal wafers. *Journal of the Less Common Metals* **1988**, *143*, 71-75.

(25) McGregor, D.; Unruh, T.; McNeil, W. Thermal neutron detection with pyrolytic boron nitride. *Nuclear Instruments and Methods in Physics Research Section A* **2008**, *591*, 530–533.

(26) Pierson, H. O. Boron nitride composites by chemical vapor deposition. *Journal of Composite Materials* **1975**, *9*, 228-240.

(27) Rozenberg, A. S.; Sinenko, Y. A.; Chukanov, N. V. Regularities of pyrolytic boron nitride coating formation on a graphite matrix. *Journal of Materials Science* **1993**, *28*, 5528-5533.

(28) Middleman, S. The role of gas-phase reactions in boron nitride growth by chemical vapor deposition. *Materials Science and Engineering* **1993**, *163*, 135-140.

(29) Shi, Y.; Hamsen, C.; Jia, X.; Kim, K. K.; Reina, A.; Hofmann, M.; Hsu, A. L.; Zhang, K.; Li, H.; Juang, Z. Y.; Dresselhaus, M. S.; Li, L.; Kong, J. Synthesis of Few-Layer Hexagonal Boron Nitride Thin Film by Chemical Vapor Deposition. *Nano Letters* **2010**, *10*, 4134-4139.

(30) Kim, K. K.; Hsu, A.; Jia, X.; Kim, S. M.; Shi, Y.; Hofmann, M.; Nezich, D.; Rodriguez-nieva, J. F.; Dresselhaus, M.; Palacios, T.; Kong, J. Synthesis of Monolayer Hexagonal Boron Nitride on Cu Foil Using Chemical Vapor Deposition. *Nano Letters* **2012**, *12*, 161-166.

(31) Boo, J. H.; Lee, S. B.; Yu, K. S.; Kim, Y.-soo; Kim, Y. S.; Park, J. T. MOCVD of hexagonal boron nitride thin films on Si (100) using new single source precursors. *Journal of the Korean Physical Society* **1999**, *34*, 532–537.

(32) Moore, A. W.; Strong, S. Variations in the structure and morphology of pyrolytic boron nitride. *Ceramic Engineering and Science Proceedings* **1989**, *10*, 846–856.

(33) Taniguchi, T. Growth of Cubic Boron Nitride Single Crystals Using a Metal Solvent under High Pressure. *New Diamond and Frontier Carbon Technology* **2004**, *14*, 289-297.

(34) Wentorf, R. H. Synthesis of the Cubic Form of Boron Nitride. *The Journal of Chemical Physics* **1961**, *34*, 809.

(35) Taniguchi, T.; Watanabe, K. Synthesis of high-purity boron nitride single crystals under high pressure by using Ba–BN solvent. *Journal of Crystal Growth* **2007**, *303*, 525-529.

(36) Kubota, Y.; Watanabe, K.; Taniguchi, T. Synthesis of Cubic and Hexagonal Boron Nitrides by Using Ni Solvent under High Pressure. *Japanese Journal of Applied Physics* **2007**, *46*, 311-314.

(37) Ishii, T.; Sato, T. Growth of single crystals of hexagonal boron nitride. *Journal of Crystal Growth* **1983**, *61*, 689–690.

(38) Yang, P.; Prater, J.; Liu, W.; Glass, J.; Davis, R. The formation of epitaxial hexagonal boron nitride on nickel substrates. *Journal of Electronic Materials* **2005**, *34*, 1558–1564.

(39) Abdulrahman, R. F.; Hendry, A. The Solubility of Nitrogen in Liquid Pure Nickel. *Metallurgical and Materials Transactions B* **2001**, *32*, 1095-1101.

(40) Kowanda, C.; Speidel, M. . Solubility of nitrogen in liquid nickel and binary Ni–Xi alloys (Xi=Cr, Mo,W, Mn, Fe, Co) under elevated pressure. *Scripta Materialia* **2003**, *48*, 1073-1078.

(41) Kubota, Y.; Watanabe, K.; Tsuda, O.; Taniguchi, T. Deep ultraviolet light-emitting hexagonal boron nitride synthesized at atmospheric pressure. *Science* **2007**, *317*, 932-4.

(42) Abdulrahman, R.; Hendry, A. Solubility of nitrogen in liquid nickel-based alloys. *Metallurgical and Materials Transactions B* **2001**, *32*, 1103–1112.

(43) Kubota, Y.; Watanabe, K.; Tsuda, O.; Taniguchi, T. Hexagonal Boron Nitride Single Crystal Growth at Atmospheric Pressure Using Ni−Cr Solvent. *Chemistry of Materials* **2008**, *20*, 1661-1663.

(44) Nash, P. Ni-Cr. In *ASM Handbook, Volume 3 - Alloy Phase Diagrams*; Baker, H.; Okamoto, H., Eds.; ASM International, 1992.

(45) Liao, P. K.; Spear, K. E. B-Ni. In *ASM Handbook, Volume 3 - Alloy Phase Diagrams*; Baker, H.; Okamoto, H., Eds.; ASM International, 1992; Vol. 30.

(46) Chakrabarti, D.; Laughlin, D. The B- Cu (Boron- Copper) system. *Journal of Phase Equilibria* **1982**, *3*, 45–48.

(47) Bondar, A.; MSIT B-Cr-Ni (Boron-Chromium-Nickel). In *Landolt-Börnstein New Series IV/11C3*; Effenberg, G.; Ilyenko, S., Eds.; Springer Berlin Heidelberg: Berlin, Heidelberg, 2007; Vol. 11C3, pp. 153-167.

(48) Schroder, R. R.; Muller, M. B1.17 Microscopy: Electron (SEM and TEM). In *Encyclopedia of Chemical Physics and Physical Chemistry, Vol II*; Moore, J. H.; Spencer, N. D., Eds.; 2001; pp. 1-35.

(49) Prince, E. B1.8 Diffraction: x-ray, neutron and electron. In *Encyclopedia of Chemical Physics and Physical Chemistry, Vol II*; Moore, J. H.; Spencer, N. D., Eds.; 2001; pp. 1-25.

(50) Housecroft, C.; Sharpe, A. *Inorganic Chemistry, 3rd Edition*; Pearson Education Limited, 2008; pp. 100-101.

(51) Gorbachev, R. V.; Riaz, I.; Nair, R. R.; Jalil, R.; Britnell, L.; Belle, B. D.; Hill, E. W.; Novoselov, K. S.; Watanabe, K.; Taniguchi, T.; Geim, A. K.; Blake, P. Hunting for monolayer boron nitride: optical and Raman signatures. *Small* **2011**, *7*, 465-8.

(52) Arutyunyan, N. R.; Obraztsova, E. D.; Silly, M.; Jaffrennou, P.; Attal-Tretout, B.; Loiseau, A.; Chuvilin, a. L. Thermal effects in Raman spectra of hexagonal boron nitride and nanotube-containing boron nitride soot. *Physica Status Solidi (B)* **2006**, *243*, 3316-3319.

(53) Chubarov, M.; Pedersen, H.; Högberg, H.; Darakchieva, V.; Jensen, J.; Persson, P. O. Å.; Henry, A. Epitaxial CVD growth of sp2-hybridized boron nitride using aluminum nitride as buffer layer. *Physica Status Solidi (RRL) - Rapid Research Letters* **2011**, *5*, 397-399.

(54) Babich, I. L. Raman Spectrum of Hexagonal Boron Nitride. *Theoretical and Experimental Chemistry* **1974**, *8*, 594-595.

(55) Watanabe, K.; Taniguchi, T. Jahn-Teller effect on exciton states in hexagonal boron nitride single crystal. *Physical Review B* **2009**, *79*, 1-4.

(56) Jin, M.-S.; Kim, N.-O. Photoluminescence of Hexagonal Boron Nitride (h-BN) Film. *Journal of Electrical Engineering and Technology* **2010**, *5*, 637-639.

(57) Chen, H.; Chen, Y.; Liu, Y.; Xu, C.; Williams, J. Light emission and excitonic effect of boron nitride nanotubes observed by photoluminescent spectra. *Optical Materials* **2007**, *29*, 1295-1298.

(58) Filonenko, N.; Mishina, L. Chemical-Etching Study of the Structure of Boron Nitride Crystals. *Soviet Physics Doklady* **1971**, *15*, 1085.

(59) Harris, S. J.; Weiner, A. M.; Doll, G. L.; Meng, W. J. Selective chemical etching of hexagonal boron nitride compared to cubic boron nitride. *Journal of Materials Research* **1997**, *12*, 412–415.

(60) Patel, A.; Bahl, O. Evidence of screw dislocations in graphite. *British Journal of Applied Physics* **1965**, *16*, 169-171.

(61) Kamler, G.; Weyher, J.; Grzegory, I.; Jezierska, E.; Wosiski, T. Defect-selective etching of GaN in a modified molten bases system. *Journal of Crystal Growth* **2002**, *246*, 21-24.

(62) Lessoff, H.; Gorman, R. A eutectic dislocation etch for gallium arsenide. *Journal of Electronic Materials* **1984**, *13*, 733-739.

(63) Weyher, J. L.; Lazar, S.; Borysiuk, J.; Pernot, J. Defect-selective etching of SiC. *Physica Status Solidi (a)* **2005**, *202*, 578-583.

(64) Weyher, J.; Brown, P.; Rouviere, J.; Wosinski, T.; Zauner, A.; Grzegory, I. Recent advances in defect-selective etching of GaN. *Journal of Crystal Growth* **2000**, *210*, 151–156.

(65) Markov, I. V. *Crystal Growth for Beginners: Fundamentals of Nucleation, Crystal Growth and Epitaxy*; World Scientific, 1995.

(66) Leist, J. with Momentive Performance Materials; personal communication **2011**.

(67) Alem, N.; Erni, R.; Kisielowski, C.; Rossell, M.; Gannett, W.; Zettl, A. Atomically thin hexagonal boron nitride probed by ultrahigh-resolution transmission electron microscopy. *Physical Review B* **2009**, *80*, 1-7.

(68) Odlyzko, M.; Mkhoyan, K. TEM Simulations of Tilted Atomically Thin Hexagonal Boron Nitride Sheets. *Microscopy and Microanalysis* **2011**, *17*, 1460-1461.

(69) Weyher, J.; Kelly, J. Defect-selective etching of semiconductors. In *Springer Handbook of Crystal Growth*; Dhanaraj, G.; Byrappa, K.; Prasad, V.; Dudley, M., Eds.; Springer Berlin Heidelberg, 2010; pp. 1453-1476.

(70) Soga, T.; Jimbo, T.; Umeno, M. Low etch pit density GaAs on Si grown by metalorganic chemical vapor deposition. *Applied Physics Letters* **1990**, *56*, 1433-35.

(71) Austerman, S. B.; Myron, S. M.; Wagner, J. W. Growth and characterization of graphite single crystals. *Carbon* **1967**, *5*, 549-557.

(72) Amelinckx, S.; Delavignette, P. Dislocation loops due to quenched-in point defects in graphite. *Physical Review Letters* **1960**, *5*, 50-51.

(73) Amelinckx, S.; Delavignette, P. Electron optical study of basal dislocations in graphite. *Journal of Applied Physics* **1960**, *31*, 2126-2135.